

**From the holdings of the Department of Special Collections,
Princeton University Library, Princeton, NJ**

These documents are either in the public domain, or can only be used for educational and research purposes (“Fair use”) as per U.S. Copyright law (text below). By accessing this file, all users agree that their use falls in the public domain or within fair use as defined by the copyright law. We do not charge any permission or usage fees for the publication of images of material in our collections, including those provided by Princeton University Library, via our website, catalog, or directly from staff.

For more information regarding copyright, credit, and citation please review the information on the [Copyright, Credit and Citation Guidelines](#) page of our website. If you have any questions, including how to order higher-quality images from the collection, contact Special Collections Public Services via our [Ask Us! Form](#).

U.S. Copyright law:

The copyright law of the United States ([Title 17, §108, United States Code](#)) governs the making of photocopies or other reproductions of copyrighted material. Under certain conditions specified in the law, libraries and archives are authorized to furnish a photocopy or other reproduction. One of these specified conditions is that the photocopy or reproduction is not to be used for any purpose other than private study, scholarship, or research. If a user makes a request for, or later uses, a photocopy or reproduction for purposes in excess of fair use that user may be liable for copyright infringement. This institution reserves the right to refuse to accept a copying order if, in its judgment, fulfillment of the order would involve a violation of copyright law.

Hyperuniformity and Diffusion Spreadability of Quasiperiodic Tilings

Adam Hitin Bialus

Senior Thesis

Department of Physics

Princeton University

05/01/2023



Advisor: Professor Salvatore Torquato

Reader: Professor Paul J. Steinhardt

This paper represents my work in accordance with University regulations.

/s/ Adam

Abstract

Hyperuniform materials are characterized by an anomalous suppression of large-scale density compared to typical disordered materials, and embody all crystals and quasicrystals as well as exotic disordered varieties. Such correlated materials are endowed with novel photonic, phononic, electronic, thermal, mechanical, and diffusion properties. This work explores the hyperuniformity and antihyperuniformity in one- and two-dimensional quasiperiodic tilings and systems, and methods to extract their values of α , which are the exponents that characterize the scaling behavior of the structure factor and spectral density at small wave numbers. In addition to using the number variance $\sigma_N^2(R)$ to numerically validate previous theoretical predictions of the hyperuniform scaling properties of one-dimensional tilings, we explore for the first time, two-phase quasiperiodic packings. Using the volume-fraction variance $\sigma_V^2(R)$, we find that all two-phase systems considered belong to the same hyperuniform class as their underlying point patterns, and that the class II, III and antihyperuniform systems possess the same values of α as their point patterns. We find no advantage in using the volume-fraction variance over the number variance to extract α , since both quantities involve integrals on the spectral density and structure factor respectively, that smooth the spectral functions in similar ways. We use the long-time behavior of the spreadability - a newly introduced concept which serves as a powerful tool to characterize heterogeneous media across length scales - to extract values of α for the different two-phase systems from their time-dependent properties. We find that the Gaussian kernel of the spreadability provides smoothing of the spectral density that proves to be more robust against “microscopic-scale” oscillations than all other previously used quantities. The spreadability is found to be a more accurate tool for extracting values of α than either the number and volume-fraction variances or the spectral intensity function $Z(k)$.

Contents

1	Introduction	1
2	Background	5
2.1	Crystals, quasicrystals, and their hyperuniformity	5
2.2	Point Configurations and correlation functions	6
2.3	Number variance and definition of hyperuniformity for point patterns	8
2.4	Hyperuniformity in two-phase media	9
2.5	Spreadability	10
3	Methods	11
3.1	Generating point configurations and decoration of points	11
3.2	Calculation of number and volume-fraction variances and excess spreadability	14
4	Results	15
4.1	1D chains	15
4.1.1	Number Variance	15
4.1.2	Volume-Fraction Variance	20
4.1.3	Structure Factor	25
4.1.4	Spreadability	26
4.1.5	Logarithmic Derivative of the Excess Spreadability	30
4.2	2D Penrose tiling	35
5	Discussion	41

1 Introduction

Hyperuniform point configurations posses *number density* fluctuations that are greatly suppressed in comparison to those in typical disordered point configurations. For hyperuniform systems in d -dimensional euclidean space, \mathbb{R}^d , the local number variance of points within a spherical observation window of radius R , denoted $\sigma_N^2(\mathbf{R})$, tends to 0 when scaled by the volume of the window $v_1(\mathbf{R})$, as the window volume tends to infinity:

$$\lim_{v_1(\mathbf{R}) \rightarrow \infty} \frac{\sigma_N^2(\mathbf{R})}{v_1(\mathbf{R})} = 0 \quad (1.1)$$

In Fourier space, the structure factor $S(\mathbf{k})$, which can be found via scattering experiments [1], of hyperuniform systems tends to 0 as $|\mathbf{k}| \rightarrow 0$:

$$\lim_{|\mathbf{k}| \rightarrow 0} S(\mathbf{k}) = 0. \quad (1.2)$$

When the structure factor has a power-law scaling near the origin, i.e. $S(\mathbf{k}) \sim B|\mathbf{k}|^\alpha$, hyperuniform systems are divided into three distinct hyperuniformity classes using the scaling exponent α :

$$\sigma_N^2(R) \sim \begin{cases} R^{d-1}, & \alpha > 1 \quad (\text{Class I}) \\ R^{d-1} \ln(R), & \alpha = 1 \quad (\text{Class II}) \\ R^{d-\alpha}, & (0 < \alpha < 1), \quad (\text{Class III}). \end{cases}$$

Class I is the “strongest” form of hyperuniformity, containing all perfect crystals [2], some quasicrystals [3–5], stealthy and other hyperuniform disordered ground states [6, 7], perturbed lattices and other systems [8, 9]. Class II contains some quasicrystals [4], classical disordered ground states [6, 10], zeros of the Riemann zeta function [11, 12], and a few other systems (Refs. 11, 13, 14 for more examples). Class III is the “weakest” form of hyperuniformity which contains classical disordered ground states [15], random organization models [16, 17], perfect glasses [10], and perturbed lattices [18].

The concept of hyperuniformity can also be extended to two-phase media, where hyperuniform two-phase media are characterized by anomalously large suppression of *volume fraction* fluctuations compared to garden-variety nonhyperuniform media [3, 19]. The volume fraction variance $\sigma_V^2(\mathbf{R})$ is the two-phase medium analog to the number variance of a point pattern, which measures the variance of volume of one phase with respect to the total volume within a spherical observation window. The asymptotic scaling law of the local volume fraction variance of a hyperuniform two-phase media associated with a spherical observation window is given by [19]:

$$\lim_{v_1(\mathbf{R}) \rightarrow \infty} \sigma_V^2(\mathbf{R}) v_1(\mathbf{R}) = 0. \quad (1.3)$$

The two-phase medium analog to the structure factor is the spectral density $\tilde{\chi}_V(\mathbf{k})$, which provides information on the particles’ positions and volume, and like the structure factor, can be found via scattering experiments [20, 21]. A two-phase hyperuniform medium is one whose spectral density at the origin vanishes:

$$\lim_{|\mathbf{k}| \rightarrow 0} \tilde{\chi}_V(\mathbf{k}) = 0. \quad (1.4)$$

When the spectral density scales as a power-law near the origin, i.e., $\tilde{\chi}_V(\mathbf{k}) \sim B|\mathbf{k}|^\alpha$, one can use α to classify hyperuniform systems:

$$\sigma_V^2(R) \sim \begin{cases} R^{-(d+1)}, & \alpha > 1 \quad (\text{Class I}) \\ R^{-(d+1)} \ln(R), & \alpha = 1 \quad (\text{Class II}) \\ R^{-(d+\alpha)}, & (0 < \alpha < 1), \quad (\text{Class III}). \end{cases}$$

There is a noteworthy advantage of using the Fourier-space functions $S(\mathbf{k})$ and $\tilde{\chi}_V(\mathbf{k})$ over using the real-space functions $\sigma_N^2(R)$ and $\sigma_V^2(R)$ to classify hyperuniform systems. Notice that for class II and III hyperuniform systems, the value of the exponent α can be found from the asymptotic scaling properties of the real-space functions $\sigma_N^2(R)$, and $\sigma_V^2(R)$. Yet, for class I systems, the real-space local number or volume-fraction variance functions asymptotically scale in the same way regardless of the value of α , namely R^{d-1} for the number variance, and $R^{-(d+1)}$ for the volume fraction variance. In other words, one cannot distinguish between degrees of hyperuniformity of class I systems from these real-space function, like certain classes of substitution tilings, or perfect glasses which can take an arbitrary values of α [5,10]. On the other hand, since the structure factor or spectral density scale as $B|\mathbf{k}|^\alpha$ near the origin, the value of the exponent α is readily available for any hyperuniformity class.

The newly introduced spreadability concept, developed by Torquato [22], serves as a link between time-dependent diffusive processes and the microstructure of heterogeneous media across different length scales [22–25]. Consider the mass transfer problem in a two-phase medium as a function of time. Assume that initially the solute is distributed uniformly only in phase 2 which occupies a volume fraction ϕ_2 , and absent from phase 1 which occupies a volume fraction ϕ_1 . Assume also that both phases have the same diffusion coefficient D at all times. The time-dependant fraction of total solute that is present in phase 1 is termed the *spreadability* $\mathcal{S}(t)$, as it is a measure of the spreadability of information from phase 2 to phase 1. Torquato expanded the original work done in \mathbb{R}^3 by Prager [26] and showed that in any dimension d , the spreadability is related to the microstructure in direct space through the autocovariance function $\chi_V(\mathbf{r})$ or in Fourier space via the spectral density $\tilde{\chi}_V(\mathbf{k})$ [22]:

$$\begin{aligned}\mathcal{S}(\infty) - \mathcal{S}(t) &= \frac{1}{(4\pi Dt)^{d/2}\phi_2} \int_{\mathbb{R}^d} \chi_V(\mathbf{r}) e^{-r^2/4Dt} d\mathbf{r} \\ &= \frac{1}{(2\pi)^d \phi_2} \int_{\mathbb{R}^d} \tilde{\chi}_V(\mathbf{k}) e^{-k^2 Dt} d\mathbf{k}.\end{aligned}\tag{1.5}$$

Here $\mathcal{S}(\infty) = \phi_1$, and $\mathcal{S}(\infty) - \mathcal{S}(t)$ is called the *excess spreadability*. The spreadability is one of the rare instances where the transport properties of two-phase media are exactly described by the first two correlation functions, namely ϕ_2 and the two point statistics $\chi_V(\mathbf{r})$ or $\tilde{\chi}_V(\mathbf{k})$ [27]. Torquato then demonstrated that the small-, intermediate-, and long-time behaviors of $\mathcal{S}(t)$ are directly determined by the small-, intermediate-, and large-scale structural features of the material [22]. Specifically, in instances where the spectral density behaves as a power law near the origin, $\lim_{|\mathbf{k}| \rightarrow 0} \tilde{\chi}_V(\mathbf{k}) \sim |\mathbf{k}|^\alpha$ he showed that, the long time excess spreadability behaves as $\sim t^{-(d+\alpha)/2}$. Hence, the spreadability serves as a dynamical tool to probe and categorize all translationally invariant two-phase media using their long-time scaling. The spreadability can be used to classify systems of any hyperuniformity class, but also ordered and disordered stealthy systems ($\alpha = \infty$), nonhyperuniform systems ($\alpha = 0$), and antihyperuniform systems ($-d < \alpha < 0$). Moreover, as a physical, measurable, quantity, the spreadability can be used to quantify microstructures when scattering information is not available [24]. Note that the Gaussian functions included in equation (1.5) reveal that the spreadability can be regarded as a Gaussian smoothing of either the autocovariance or spectral density. We will exploit this fact to smooth-out “microscopic-scale” oscillations of the spectral density to extract values of α that agree more closely with theory than those extracted using the number and volume-fraction variances.

Hyperuniformity generalizes the traditional concept of long-range order and allows for the classification of all perfect crystals, perfect quasicrystals, and special disordered systems [2,3,27]. Hyperuniform states of matter play a vital role in a plethora of applied and theoretical disciplines such as photonic and phononic band-gap properties [28–32], antenna or laser design [33], thermal properties of stealthy

systems [34, 35], transport properties and critical currents in superconductors [36], diffusion processes in two-phase media [22–24], and pure mathematics [37–40]. System have also been numerically produced with desirable hyperuniform properties [41]

Quasicrystals are a unique state of matter that possesses long-range orientational order, but lacks translational symmetry. Quasicrystalline structures were first observed in rapidly cooled aluminium-manganese alloys via diffraction experiments. The diffraction pattern featured sharp Bragg peaks, suggesting long-range order, but exhibited ten-fold rotational symmetry, which is a disallowed crystallographic group, inconsistent with periodicity [42, 43]. The discovery of quasicrystalline structures led to a generalized concept of long-range order which is orientaional and not periodic. Specifically that a translationally ordered structure possesses scattering amplitudes composed of a discrete sum of Bragg peaks [44]. Since their discovery, quasicrystals have been used in a verity of practical applications. The control in a quasicrystal's aperiodicity has potential for unprecedented control over the near- and far-field spectral properties of photonic devices [45, 46], and since photonic quasicrystals exhibit band gaps, they are suitable for the same scientific and technological applications as photonic crystals [47–51].

Numerical and analytical calculations of the number variance and structure factor suggest evidence that hyperuniform quasicrystals exist in both class I and II [3, 29, 52, 53]. Oğuz et al. (2017) [4], explored the projection of points from a two-dimensional integer lattice onto a line of slope τ , producing Fibonacci quasicrystals. They concluded that depending on the width of the projection window, two different hyperuniformity exponents are attainable, namely $\alpha = 3$ and $\alpha = 1$, corresponding to class I and II respectively. They compared the results to analytical calculations of the number variance for the class I projection windows, and suggested a method to numerically compute the number variance for the class II projection windows. Oğuz et al.(2018), expanded this work from 2017 to consider 1-dimensional substitution tilings (Section 3). Here they conjectured an analytical form for the hyperuniformity scaling exponent for such tilings, and showed that it can take values in the interval $(-1, 3]$ [5], which they confirmed with numerical simulations. Lin et al., studied two-dimensional quasicrystals produced via a projection from a five-dimensional hypercubic lattice [54]. They showed that the degree of hyperuniformity in these two-dimensional quasicrystals, depends on the system's local isomorphism class [54]. While the properties of quasicrystals, hyperuniformity and other, draw much attention, quasicrystals in the form of a two-phase medium have never been studied.



Figure 1: An example of the first few links in a Fibonacci chain.

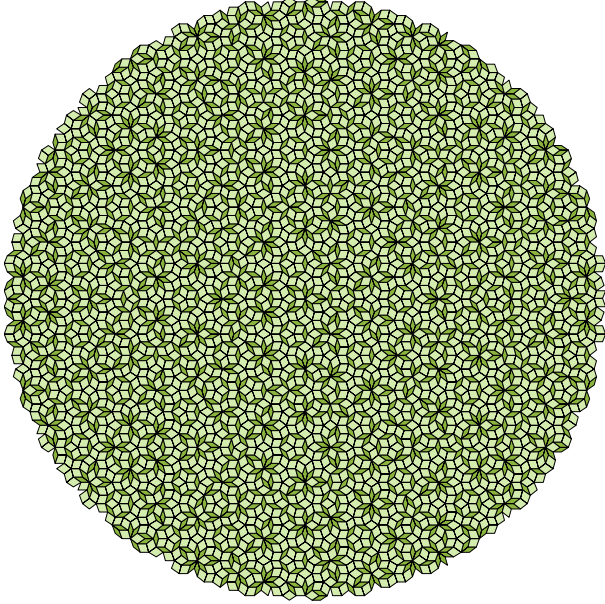


Figure 2: A portion of a two-dimensional Penrose tiling approximation generated using Ref 55.

In this work, we study the properties of periodic approximants of one- and two-dimensional quasiperiodic tilings. Previous investigations revealed that the integrated intensity function $Z(k)$, can be used to extract the hyperuniformity scaling exponent α of one-dimensional tilings whose structure factor consists of a dense set of Bragg peaks [4]. It was also found that α can be predicted given knowledge of how the systems were formed [5]. Moreover, numerical calculations of the number variance suggest that some two-dimensional quasicrystals are class I hyperuniform [3].

Using the excess spreadability, we wish to improve previous estimations of α , and importantly, to extract precise values of α for systems of any hyperuniform and nonhyperuniform classes including antihyperuniform, with no prior knowledge of how the systems were constructed. To benchmark our computational methods, we begin by using them to reproduce and validate previous results. Moreover, we endeavor to explore the validity of theoretical conjectures [5] on systems that have yet to be done numerically.

In one dimension (1D), seven systems are generated via the substitution method, described in detail in Section 3, with between $N = 10^3$ to $N = 10^7$ particles, that span all hyperuniform or nonhyperuniform systems including antihyperuniform. In two dimensions (2D), a periodic approximation of a Penrose quasicrystal is produced via the Generalized Dual Method (Section 3), with between $N \approx 100$ to $N \approx 10^6$ particles. The point configurations are then mapped into systems of nonoverlapping identical particles called packings, for which the spectral density is trivially related to the structure factor (Section 3). The spectral densities are then used to compute the excess spreadability $\mathcal{S}(\infty) - \mathcal{S}(t)$ via equation (1.5), and the long-time behavior of the spreadability can be used to extract the hyperuniformity scaling exponent α , as detailed in Section 3. We use three different quantities to analyze the different packings described in Section 3: the volume-fraction variance, $Z(k)$, and the excess spreadability. Values of α extracted via the volume-fraction variance perform just as well as those extracted using the number variance when compared to theoretical predictions. As a benchmark for the spreadability, we report values of α for the 1D systems that are within 1% of theoretical results for the class I, III, and antihyperuniform systems, and within 4% for class II. Given that we have established the superiority of the spreadability to extract

the exponent α for either hyperuniform or nonhyperuniform media, we expect it will be a valuable tool to study the large-scale structural properties of other nontrivial two-phase media. Furthermore, the results show that theoretical conjectures [5] are in close agreement with some systems here that have yet to be done numerically. We also find that using the spreadability to extract α is more robust to oscillations on lengths of order of a tile size (“microscopic-scale”) and on length scales much larger than a tile but much smaller than the system size (“global-scale”), then when using the functions $\sigma_N^2(\mathbf{R})$ and $\sigma_V^2(\mathbf{R})$. Both $\sigma_N^2(\mathbf{R})$ and $\sigma_V^2(\mathbf{R})$ involve integrals on the spectral density and structure factor, respectively, that smooth the spectral functions in similar ways. Yet, while the integrals mentioned above involve functions that decay as an inverse power law [2], the Gaussian kernel of equation (1.5) of the Fourier representation of the spreadability decays superexponentially fast [22], and therefore, it provides better smoothing, which leads to values of α that match theoretical predictions better compared to the variances. For the 2D Penrose medium, we report for the first time, to the best of our knowledge, the value of α for the 2D Penrose quasicrystal. We also observe that the smoothing operation of the spreadability is superior to that of the integrated intensity function $Z(k)$. We conclude that there is no significant advantage of using the volume-fraction variance over the number variance to extract values of α . Moreover, we find that the spreadability is more accurate than $\sigma_N^2(R)$, and $\sigma_V^2(R)$ and it serves as a powerful dynamic tool to extract values of α of quasiperiodic two-phase media of any hyperuniform or nonhyperuniform classes, including antihyperuniform.

This thesis is organised as follows: Section 2 provides mathematical definitions and preliminaries for hyperuniformity, spreadability, and quasicrystals. Section 3, discusses the one- and two-dimensional models used in the study, their creation methods, and the procedures used to extract α from the local number and volume-fraction variances, as well as the excess spreadability. Results are reported in Section 4, and Section 5 provides conclusions and directions for further work.

2 Background

2.1 Crystals, quasicrystals, and their hyperuniformity

A Bravais lattice is a periodic point configuration which specifies the geometric structure in which the crystal units are arranged. A (d -dimensional) Bravais lattice is defined as all the points with vectors \mathbf{R} of the form [56]:

$$\mathbf{R} = \sum_{i=1}^d n_i \mathbf{a}_i,$$

where \mathbf{a}_i are called primitive vectors and they form a basis for \mathbb{R}^d , and $n_i \in \mathbb{Z}$. A primitive unit cell is then defined as a region in space that when translated by any primitive vector, fills out all of space without overlapping or leaving voids. The choice of a primitive unit cell is not unique and many such cells can be found for any Bravais lattice. A Bravais lattice can be characterized by its symmetries which are all rigid operations that map the lattice back into itself and are called the symmetry group or space group of the lattice. These include translation by primitive vectors, rotations, reflections, inversions, and combinations of these transformations.

A crystal is described by its underlying lattice structure and the arrangement of components within each primitive cell. The components can be atoms, molecules, etc. The symmetry groups of the crystal structure depend both on the symmetries of the lattice and of the components. Both perfect lattices and their associated perfect crystals, are hyperuniform of class I [2].

Quasicrystalline systems posses certain types of rotational symmetries that are forbidden in perfect crystals since they require the breaking of translational symmetry. For example, five-fold symmetry in two

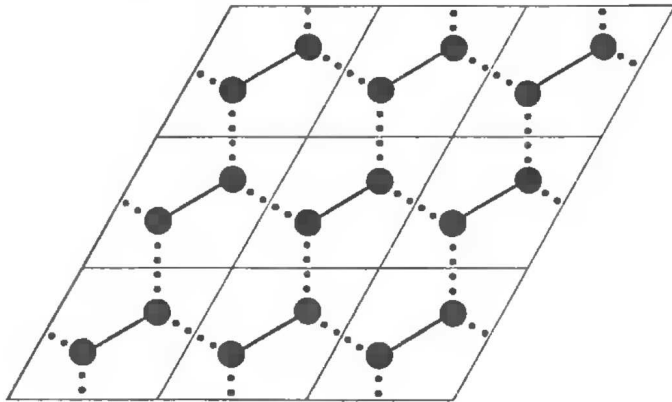


Figure 3: An example of a honeycomb crystal structure with a two-point basis. the basis points are connected via the solid lines and connected between cells via the dashed lines. Figure reproduced from Ref 56

dimensions and icosahedral symmetry in three dimension [43] [57].

2.2 Point Configurations and correlation functions

Consider an N -point configuration $\mathbf{r}^N \equiv \mathbf{r}_1, \mathbf{r}_2, \dots, \mathbf{r}_N$ in some volume V . The microscopic number density at \mathbf{x} is given as

$$n(\mathbf{x}) = \sum_{i=1}^N \delta(\mathbf{x} - \mathbf{r}_i), \quad (2.1)$$

where $\delta(\mathbf{x})$ is the Dirac delta function. The configuration is statistically characterized by the specific probability density function $P_N(\mathbf{r}^N)$, where $P_N(\mathbf{r}^N)d\mathbf{r}^N$ is the probability of finding point 1 in a volume element $d\mathbf{r}_1$, point 2 in a volume element $d\mathbf{r}_2$, and so on. The reduced generic density $\rho_n(\mathbf{r}^n)$ is defined as

$$\rho_n(\mathbf{r}^n) = \frac{N!}{(N-n)!} \int_V \cdots \int_V P_N(\mathbf{r}^N) d\mathbf{r}^{N-n}, \quad (2.2)$$

where $d\mathbf{r}^{N-n} \equiv d\mathbf{r}_{n+1}d\mathbf{r}_{n+2}\dots d\mathbf{r}_N$. Then $\rho_n(\mathbf{r}^n)$ is proportional to the joint probability distribution of finding any n particles with configuration \mathbf{r}^n in volume element $d\mathbf{r}^n$. A point pattern is statistically homogeneous, or translationally invariant, if the reduced generic density $\rho_n(\mathbf{r}^n)$ is invariant under a translation by \mathbf{y} for any vector \mathbf{y} in \mathbb{R}^d , i.e.,

$$\rho_n(\mathbf{r}_1, \mathbf{r}_2, \dots, \mathbf{r}_n) = \rho_n(\mathbf{r}_1 + \mathbf{y}, \mathbf{r}_2 + \mathbf{y}, \dots, \mathbf{r}_n + \mathbf{y}), \quad (2.3)$$

which implies that $\rho_n(\mathbf{r}^n)$ depends only on the relative displacements between particles [27, 58]. Taking the relative displacement with respect to \mathbf{r}_1 gives:

$$\rho_n(\mathbf{r}^n) = \rho_n(\mathbf{r}_{12}, \mathbf{r}_{13}, \dots, \mathbf{r}_{1n}), \quad (2.4)$$

where $\mathbf{r}_{ij} = \mathbf{r}_j - \mathbf{r}_i$. The one-particle function ρ_1 is equal to the constant number density of particles ρ :

$$\rho_1(\mathbf{r}_1) = \rho = \lim_{N, V \rightarrow \infty} \frac{N}{V}, \quad (2.5)$$

and the limit of $N, V \rightarrow \infty$ is referred to as the *thermodynamic limit*. Using this limit, one can define the n-particle correlation function,

$$g_n(\mathbf{r}^n) = \frac{\rho_n(\mathbf{r}^n)}{\rho^n}. \quad (2.6)$$

Notice that for systems with no long range order and with particles that are mutually far from one another the function $\rho_n(\mathbf{r}^n)$ approaches ρ^n , which then implies $g_n(\mathbf{r}^n) \rightarrow 1$. g_n is thus a measure of the degree of correlation between the particles in the system, where $g_n(\mathbf{r}^n) = 1$ corresponds to no spatial correlation. The pair correlation function $g_2(\mathbf{r}_{12})$ is defined as

$$g_2(\mathbf{r}_{12}) = \frac{\rho_2(\mathbf{r}_{12})}{\rho^2}, \quad (2.7)$$

and the total correlation function $h(\mathbf{r}_{12})$ as

$$h(\mathbf{r}_{12}) = g_2(\mathbf{r}_{12}) - 1. \quad (2.8)$$

The interpretation of $g_2(\mathbf{r}_{12})$ is the conditional probability of finding a particle center in the volume $s_1(R)dr$, given there is a particle at the origin. Here

$$s_1(r) = \frac{2\pi^{d/2} r^{d-1}}{\Gamma(d/2)}, \quad (2.9)$$

is the surface area of a d -dimensional sphere of radius r , and $\Gamma(x)$ is the gamma function. The spectral function named the *structure factor* $S(\mathbf{k})$ can be defined in terms of the Fourier transform of the total correlation function $\tilde{h}(\mathbf{k})$:

$$S(\mathbf{k}) = 1 + \rho \tilde{h}(\mathbf{k}), \quad (2.10)$$

where $\tilde{h}(\mathbf{k})$ is the Fourier transform of the total correlation function, and the d -dimensional Fourier transform is defined here as

$$\tilde{f}(\mathbf{k}) = \int_{\mathbb{R}^d} f(\mathbf{r}) e^{-i\mathbf{k}\cdot\mathbf{r}} d\mathbf{r}, \quad (2.11)$$

and the inverse Fourier transform is

$$f(\mathbf{r}) = \frac{1}{(2\pi)^d} \int_{\mathbb{R}^d} \tilde{f}(\mathbf{k}) e^{i\mathbf{k}\cdot\mathbf{r}} d\mathbf{k}. \quad (2.12)$$

The structure factor is proportional to the intensity of radiation scattered from the system and it is therefore possible to observe it from scattering experiments [1]. The set of points \mathbf{k} is a Bravais lattice called the reciprocal lattice which satisfies

$$e^{i\mathbf{k}\cdot\mathbf{r}} = 0, \quad (2.13)$$

where \mathbf{r} is a point of the original lattice. Importantly, for any dimension, the reciprocal lattice vectors satisfy

$$\mathbf{b}_i \cdot \mathbf{a}_j = 2\pi\delta_{ij}, \quad (2.14)$$

where δ_{ij} is the Kronecker delta. For a single periodic configuration of points, the the scattering intensity function $\mathbb{S}(\mathbf{k})$ is given by:

$$\mathbb{S}(\mathbf{k}) = \frac{|\sum_{j=1}^N e^{-i\mathbf{k}\cdot\mathbf{r}_j}|^2}{N}, \quad (2.15)$$

which is identical to the structure factor $S(\mathbf{k})$, excluding its value at $\mathbf{k} = 0$ (forward scattering) [58].

The integrated intensity function $Z(k)$, which is related to the structure factor via [4]

$$Z(k) = \int_0^k S(\mathbf{q}) s_d q^{d-1} dq, \quad (2.16)$$

smooths the structure factor. Therefore, $Z(k)$ is useful when the structure factor is discontinuous around the origin and one cannot properly define α , like in quasicrystals [4]. It was shown that in 1D quasicrystals, while the structure factor is discontinuous, $Z(k)$ is bounded near the origin by functions of the form:

$$c_- k^{\alpha+1} \leq Z(k) \leq c_+ k^{\alpha+1}, \quad (2.17)$$

where $c_{+/-}$ are constants and $c_- \leq c_+$ [4].

2.3 Number variance and definition of hyperuniformity for point patterns

A hyperuniform point pattern is one in which the number variance $\sigma_N^2(R) \equiv \langle N(R)^2 \rangle - \langle N(R) \rangle^2$ of particles in a spherical observation window of radius R grows slower than the the window volume in the large- R limit (slower than R^d). For a general translationally invariant point configuration in \mathbb{R}^d , the local number variance can be expressed exactly by the pair correlation functions [2]:

$$\sigma_N^2(\mathbf{R}) = \langle N(\mathbf{R}) \rangle \left[1 + \rho \int_{\mathbb{R}^d} h(\mathbf{r}) \alpha_2(\mathbf{r}; \mathbf{R}) d\mathbf{r} \right], \quad (2.18)$$

or in Fourier space using the structure factor [2]:

$$\sigma_N^2(\mathbf{R}) = \langle N(\mathbf{R}) \rangle \left[\frac{1}{(2\pi)^d} \int_{\mathbb{R}^d} S(\mathbf{k}) \tilde{\alpha}_2(\mathbf{k}; \mathbf{R}) d\mathbf{k} \right]. \quad (2.19)$$

The number variance can also be written in terms of the integrated intensity function [4]:

$$\sigma_N^2(R) = -\rho v_1(R) \left[\frac{1}{(2\pi)^d} \int_0^\infty Z(k) \frac{\partial \tilde{\alpha}_2(k; R)}{\partial k} dk \right]. \quad (2.20)$$

Here

$$\alpha_2(\mathbf{r}; \mathbf{R}) = \frac{v_2^{\text{int}}(\mathbf{r}; \mathbf{R})}{v_1(\mathbf{R})} \quad (2.21)$$

is called the scaled intersection volume function, and

$$v_2^{\text{int}}(\mathbf{r}; \mathbf{R}) = \int_{\mathbb{R}} w(\mathbf{r} + \mathbf{x}_0; \mathbf{R}) w(\mathbf{x}_0; \mathbf{R}) d\mathbf{x}_0 \quad (2.22)$$

is the intersection volume of two windows with identical orientations whose centers are separated by a displacement vector \mathbf{r} , and $\tilde{\alpha}_2(\mathbf{r}; \mathbf{R})$ is the Fourier transform of $\alpha_2(\mathbf{r}; \mathbf{R})$ which is strictly positive. For finite sized windows, equation (2.18) converges for bounded $h(\mathbf{r})$ since $\alpha_2(\mathbf{r}; \mathbf{R})$ has finite support, and for infinitely large windows, $\alpha_2(\mathbf{r}; \mathbf{R}) = 1$ which then requires $h(\mathbf{r})$ to decay faster than $|\mathbf{r}|^{-d}$. In the case of spherical windows, the function $v_1(\mathbf{R})$ is given as the volume of a d -dimensional spherical window of radius R :

$$v_1(R) = \frac{\pi^{d/2}}{\Gamma(1 + d/2)} R^d. \quad (2.23)$$

Moreover, the scaled intersection volume $\alpha_2(\mathbf{r}; \mathbf{R})$ has the following integral formula:

$$\alpha_2(r; R) = c(d) \int_0^{\cos^{-1}[r/(2R)]} \sin^d(\theta) d\theta, \quad (2.24)$$

where

$$c(d) = \frac{2\Gamma(1+d/2)}{\pi^{1/2}\Gamma[(d+1)/2]}. \quad (2.25)$$

For spherical windows in the first two dimensions, $\alpha_2(\mathbf{r}; \mathbf{R})$ is given by the following closed formulae [59]:

$$\begin{aligned} \alpha_2(r; R) &= \left[1 - \frac{1}{2R}\right] \Theta(2R - 1) \quad (d = 1) \\ \alpha_2(r; R) &= \frac{2}{\pi} \left[\cos^{-1}\left(\frac{r}{2R}\right) - \frac{r}{2R} \left(1 - \frac{r^2}{4R^2}\right)^{1/2} \right] \Theta(2R - r) \quad (d = 2), \end{aligned} \quad (2.26)$$

where $\Theta(x)$ is the Heaviside step function. It is also possible to then write the Fourier transform of $\alpha_2(\mathbf{r}; \mathbf{R})$ as

$$\tilde{\alpha}_2(k, R) = 2^d \pi^{d/2} \Gamma(1 + d/2) \frac{[J_{d/2}(kR)]^2}{k^d}, \quad (2.27)$$

where $J_{d/2}(kR)$ is the Bessel function of the first kind. From equations (2.19) and (2.20), it follows [2,15] that when the structure factor goes to 0 continuously at the origin. i.e., $S(\mathbf{k}) \sim |\mathbf{k}|^\alpha$ the number variance asymptotically scales as given in equation (1.3).

Similarly to Ref 2, to smooth-out numerical noise and “microscopic-scale” oscillations, it is useful to define a running average of the function $\sigma_N^2(R)R^{\beta_N}$ where β_N is chosen such that $\sigma_N^2(R)R^{\beta_N}$ asymptotically scales as a constant. The running average of a function $f(x)$ is defined here as

$$RA[f](x) = \frac{1}{x - x_{\min}} \int_{x_{\min}}^x f(x) dx, \quad (2.28)$$

and we define the function $\Lambda_N(R)$ as

$$\Lambda_N(R) \equiv RA[\sigma_N^2(R)R^{\beta_N}]. \quad (2.29)$$

2.4 Hyperuniformity in two-phase media

A two-phase medium is a partition of space into two disjoint regions called phases, with boundaries that are known only probabilistically [27]. Let phase one occupy a volume fraction ϕ_1 and phase two occupy a volume fraction $\phi_2 = 1 - \phi_1$. The two-phase medium can be characterized by the n-point correlation functions

$$S_n^{(i)}(\mathbf{x}_1, \dots, \mathbf{x}_n) \equiv \langle \mathcal{I}^{(i)}(\mathbf{x}_1) \dots \mathcal{I}^{(i)}(\mathbf{x}_n) \rangle, \quad (2.30)$$

where $\mathcal{I}^{(i)}(\mathbf{x})$ is the indicator function of phase $i = 1, 2$, and the angular brackets indicate an ensemble average. The function $S_n^{(i)}(\mathbf{x}_1, \dots, \mathbf{x}_n)$ gives the probability of finding the vectors $\mathbf{x}_1, \dots, \mathbf{x}_n$ all in phase i . The autocovariance function $\chi_V(\mathbf{r})$ is related to the two-point correlation function $S_2^{(i)}$ by

$$\chi_V(\mathbf{r}) \equiv S_2^{(1)} - \phi_1^2 = S_2^{(2)} - \phi_2^2 \quad (2.31)$$

with statistical homogeneity. The local volume-fraction variance, $\sigma_V^2(R)$, can be written in terms of $\chi_V(\mathbf{r})$ as [3,60]:

$$\sigma_V^2(R) = \frac{1}{v(R)} \int_{\mathbb{R}^d} \chi(\mathbf{r}) \alpha_2(r; R) d\mathbf{r}. \quad (2.32)$$

Similarly to equation (2.29), we define the running average function $\Lambda_V(R)$ as $\Lambda_V(R) \equiv RA[\sigma_V^2(R)R^{\beta_V}]$, where β_V is chosen such that $\sigma_V^2(R)R^{\beta_V}$ asymptotically scales as a constant. In Fourier space equation

(2.32) is given by applying Parseval's theorem to the above equation:

$$\sigma_V^2(R) = \frac{1}{v(R)(2\pi)^d} \int_{\mathbb{R}^d} \tilde{\chi}_V(\mathbf{k}) \tilde{\alpha}_2(k; R) d\mathbf{k}. \quad (2.33)$$

Following [61], for a hyperuniform two-phase medium is one with spectral density that vanishes at the origin:

$$\lim_{|\mathbf{k}| \rightarrow 0} \tilde{\chi}_V(\mathbf{k}) = 0. \quad (2.34)$$

As with point configurations, when the spectral density behaves as a power law near the origin, i.e., $\lim_{|\mathbf{k}| \rightarrow 0} \tilde{\chi}_V(\mathbf{k}) \approx |\mathbf{k}|^\alpha$, the volume fraction variance of a hyperuniform two-phase medium scales as given in equation (1.5).

2.5 Spreadability

Recent work [22] has revealed that the time-dependent spreadability is a powerful new dynamic-based figure of merit to probe and classify the spectrum of possible microstructures of two-phase media across length scales. Consider a two phase medium where phase 1 occupies a volume fraction ϕ_1 and phase 2 occupies $\phi_2 = 1 - \phi_1$ in a random two phase medium. The time-dependent diffusion equation is given as

$$\frac{\partial c}{\partial t} = D \nabla^2 c, \quad (2.35)$$

where D is the diffusion coefficient and c is the solute concentration. Now assume that

1. $c(\mathbf{r}, t)$ vanish for all time t if \mathbf{r} is on the interface of the two phases
2. for $t = 0$, the solute is present only in phase 1.
3. the solute in the two phases has the same diffusion coefficient

Under these assumptions in \mathbb{R}^3 , Prager [26] showed that the fraction of solute diffused into phase 1 at some time t is given by:

$$S(t) = \frac{1}{(4\pi Dt)^{3/2}\phi_2} \int [\phi_2 - S_2(\mathbf{r})] e^{-\mathbf{r}^2/4Dt} d\mathbf{r}, \quad (2.36)$$

where $S_2(\mathbf{r})$ is the two-point probability function of phase 2 as defined in equation (2.30). Torquato then generalized this result to \mathbb{R}^d and showed that the quantity $\mathcal{S}(\infty) - \mathcal{S}(t)$ which is referred to as the *excess spreadability* is given by [22]:

$$\begin{aligned} \mathcal{S}(\infty) - \mathcal{S}(t) &= \frac{1}{(4\pi Dt)^{d/2}\phi_2} \int_{\mathbb{R}^d} \chi_V(\mathbf{r}) e^{-r^2/4Dt} d\mathbf{r} \\ &= \frac{d\omega_d}{(4\pi Dt)^{d/2}\phi_2} \int_0^\infty r^{d-1} \chi_V(r) e^{-r^2/4Dt} dr. \end{aligned} \quad (2.37)$$

Here ω_d is the volume of a d -dimensional sphere of unit radius and

$$\chi_V(r) = \frac{1}{\Omega} \int_\Omega \chi_V(\mathbf{r}) d\Omega, \quad (2.38)$$

is the angle averaged autocovariance function $\chi_v(\mathbf{r})$. And, in Fourier space, the excess spreadability can be written in terms of the spectral density [22]:

$$\begin{aligned}\mathcal{S}(\infty) - \mathcal{S}(t) &= \frac{1}{(2\pi)^d \phi_2} \int_{\mathbb{R}^d} \tilde{\chi}_v(\mathbf{k}) e^{-k^2 D t} d\mathbf{k} \\ &= \frac{d\omega_d}{(2\pi)^d \phi_2} \int_0^\infty k^{d-1} \tilde{\chi}_v(k) e^{-k^2 D t} dk,\end{aligned}\tag{2.39}$$

where $\tilde{\chi}_v(k)$ is the angle-averaged spectral density given by

$$\tilde{\chi}_v(k) = \frac{1}{\Omega} \int_\Omega \tilde{\chi}_v(\mathbf{k}) d\Omega.\tag{2.40}$$

Torquato also showed that for hyperuniform two-phase media where the spectral density behaves as

$$\lim_{|\mathbf{k}| \rightarrow 0} \tilde{\chi}_v(\mathbf{k}) \approx B |\mathbf{k}|^\alpha,\tag{2.41}$$

the long-time excess spreadability is given as the power-law decay of [22]

$$\mathcal{S}(\infty) - \mathcal{S}(t) = \frac{B \Gamma[(d+\alpha)/2] \phi_2}{2^d \pi^{d/2} \Gamma(d/2) (Dt/a^2)^{(d+\alpha)/2}} + o[(Dt/a^2)^{-(d+\alpha)/2}] \quad (Dt/a^2 \gg 1),\tag{2.42}$$

where a is some characteristic heterogeneity length scale and B is a microstructure-dependent coefficient. Using this last equation, it is then possible to extract α from the long time behavior of the spreadability, and so to probe the microstructure of the media.

Note that the spreadability can be regarded as a type of Gaussian smoothing of the autocovariance [cf (2.37)] or the spectral density (2.39) since they are weighted by a Gaussian integrand. The smoothing effect is expected to be especially useful for our quasicrystalline systems, since they possess not only “microscopic-scale” fluctuations but “global-scale” oscillations as well. We will show that the spreadability produces smoother plots than those of $\sigma_N^2(R)$ and $\sigma_V^2(R)$ and hence results in better estimates of α .

3 Methods

3.1 Generating point configurations and decoration of points

Following Oğus et al. [5], the 1D systems were generated via substitution rules. Starting from a single seed tile, a set of substitutions is then applied iteratively to replace it with sets of other tiles. For example, the Fibonacci chain is a particular case of the substitution rule tiling, constructed by repeated iterations of a substitution of long L and short S tiles such that $S \rightarrow L$, and $L \rightarrow LS$. This kind of substitution can be characterized by a substitution matrix \mathbf{M} given by:

$$\mathbf{M} = \begin{pmatrix} 0 & 1 \\ 1 & 1 \end{pmatrix},\tag{3.1}$$

which gives the number of S 's and L 's after a substitution by acting on the two-dimensional column vector (N_S, N_L) . A substitution rule for two tile types is characterized by the substitution matrix

$$\mathbf{M} = \begin{pmatrix} a & b \\ c & d \end{pmatrix},\tag{3.2}$$

Fibonacci chain substitution rule	
# of substitutions	Chain
0	S
1	L
2	LS
3	LSL
4	$LSLLS$
5	$LSLLSLSL$

Table 1: Construction of the Fibonacci chain out of consecutive substitutions of the type $S \rightarrow L$, and $L \rightarrow LS$

where a, b, c, d are integers. Oğuz et al., showed that by defining the length ratio $L/S = \xi$ and requiring that the substitution rule preserve this ratio one can get [5]

$$\xi = \frac{d - a + [(a - d)^2 + 4bc]^{1/2}}{2c}. \quad (3.3)$$

If one considers a decoration of each S tile with s points and each L tile with l points, then after iterating the substitution matrix m times, the number of points is given by

$$\mathcal{N}_m = (s, l) \cdot \mathbf{M}^m \cdot (n_S, n_L), \quad (3.4)$$

and the length is given by

$$\mathcal{X}_m = (1, \xi) \cdot \mathbf{M}^m \cdot (n_S, n_L). \quad (3.5)$$

Next, Oğuz et al. [5] showed that the eigenvalues and eigenvectors given by $\lambda_1, \lambda_2, \mathbf{v}_1, \mathbf{v}_2$ with $\lambda_1 > \lambda_2$ are given by

$$\begin{aligned} \lambda_1 &= a + c\xi; & \lambda_2 &= d - c\xi \\ \mathbf{v}_1 &= (b/c, \xi); & \mathbf{v}_2 &= (-\xi, 1), \end{aligned} \quad (3.6)$$

and they used these, to find the closed form formula for m iterations of \mathbf{M} :

$$\begin{aligned} \mathbf{M}^m \cdot (n_S, n_L) &= \mathbf{M}^m \cdot [n_S(1, 0) + n_L(0, 1)] \\ &= u [\lambda_1^m (cn_S + c\xi n_L) \mathbf{v}_1 + \lambda_2^m (bn_L - c\xi n_S) \mathbf{v}_2], \end{aligned} \quad (3.7)$$

with $u = 1/(b + c\xi^2)$. Using the fact that $(1, \xi) \cdot \mathbf{v}_2 = 0$, one can get that the density of tile vertices after m iterations, which is define as $\rho_m = \mathcal{N}_m / \mathcal{X}_m$ is

$$\rho_m = \bar{\rho} + \left[\frac{\xi(s\xi - l)}{b + c\xi^2} \right] \left(\frac{c\xi n_S - bn_L}{n_S + \xi n_L} \right) \left(\frac{\lambda_2}{\lambda_1} \right)^m, \quad (3.8)$$

with $\bar{\rho} = (bs + cl\xi)/(b + c\xi^2)$. Oğuz et al. [5] then conjectured a closed form formula for the hyperuniformity scaling exponent α given by the eigenvalues of the substitution matrix:

$$\alpha = 1 - 2 \frac{\ln |\lambda_2|}{\ln |\lambda_1|}. \quad (3.9)$$

In this work tilings were made using the following systems with number of particles ranging from $N = 10^3$ to $N = 10^7$:

$$\begin{aligned}
\mathbf{M} &= \begin{pmatrix} 0 & 1 \\ 1 & 1 \end{pmatrix} - \text{The Fibonacci chain} & \mathbf{M} &= \begin{pmatrix} 0 & 1 \\ 1 & 2 \end{pmatrix} - \text{the 0112 chain} \\
\mathbf{M} &= \begin{pmatrix} 3 & 5 \\ 3 & 3 \end{pmatrix} - \text{the 3533 chain} & \mathbf{M} &= \begin{pmatrix} 1 & 2 \\ 1 & 0 \end{pmatrix} - \text{the limit-periodic chain} \\
\mathbf{M} &= \begin{pmatrix} 0 & 2 \\ 2 & 2 \end{pmatrix} - \text{the 0222 chain} & \mathbf{M} &= \begin{pmatrix} 1 & 5 \\ 3 & 0 \end{pmatrix} - \text{the 1530 chain} \\
\mathbf{M} &= \begin{pmatrix} 0 & 5 \\ 5 & 5 \end{pmatrix} - \text{the 0555 chain}
\end{aligned} \tag{3.10}$$

From equation (3.9), the hyperuniformity scaling exponents α of these chains are predicted to be

$$\begin{aligned}
\alpha_{\text{Fibonacci}} &= 1 - 2 \frac{\ln |\frac{1-\sqrt{5}}{2}|}{\ln |\frac{1+\sqrt{5}}{2}|} = 3; \\
\alpha_{0112} &= 1 - 2 \frac{\ln |1 - \sqrt{2}|}{\ln |1 + \sqrt{2}|} = 3; \\
\alpha_{3533} &= 1 - 2 \frac{\ln |3 - \sqrt{15}|}{\ln |3 + \sqrt{15}|} = 1.1409; \\
\alpha_{\text{LimitPeriodic}} &= 1 - 2 \frac{\ln |-1|}{\ln |2|} = 1; \\
\alpha_{0222} &= 1 - 2 \frac{\ln |1 - \sqrt{5}|}{\ln |1 + \sqrt{5}|} = 0.6390; \\
\alpha_{1530} &= 1 - 2 \frac{\ln |-(\sqrt{61} - 1)/2|}{\ln |(\sqrt{61} + 1)/2|} = -0.652; \\
\alpha_{0555} &= 1 - 2 \frac{\ln |5/2| - (\sqrt{5} - 1)|}{\ln |5/2|(\sqrt{5} + 1)|} = -0.0793.
\end{aligned} \tag{3.11}$$

The chains are therefore divided according to their hyperuniformity class: Fibonacci, 0112 and 3533, are class I; limit-periodic is class II; 0222 is class III; and 1530 and 0555 are Antihyperuniform.

The 2D system, called a Penrose tiling, was created using the Generalized Dual Method which is a mapping from regions created by infinite intersections of straight lines, to points [54, 62]. A periodic grid is an infinite set of parallel, and straight, lines with equal spacings between them. One can then label each line by $n \in \mathbb{Z}$ according to its ordinal position in the grid. Five of these grids are then stacked one atop the other with the i th grid oriented normal to $\mathbf{r}_i = (\cos[2\pi i/5], \sin[2\pi i/5])$, and each grid is displaced by some phase γ_i from the origin. The grids partition space into open regions which can be labeled uniquely by the five integers $\mathbf{K} \equiv (k_0, k_1, \dots, k_4)$. Each point \mathbf{x} in some open region, it will lie between the lines k_i and $k_i + 1$ of the i th grid. These open regions \mathbf{K} are then mapped to the vertices \mathbf{t} of a tiling by the transformation $\mathbf{t} = \sum_{i=0}^4 k_i \mathbf{r}_i$. Here we explore tilings with number of vertices ranging between $N \approx 100$ to $N \approx 10^6$.

In order to probe the microstructure of the systems described above using the excess spreadability and volume-fraction variance, we map the one- and two-dimensional point configurations into packings. Packings can be viewed as two-phase media, where phase V_1 is the void (pore) space between the particles,

and the particle phase V_2 is the space occupied by the particles [27]. To map tilings into two-phase media, the vertices of each tile are decorated by rods in 1D, and circular disks in 2D, of radius a centered at the vertices, where a is chosen such that the particles do not overlap. The volume fraction of phase 2, ϕ_2 , of a packing is given as $\phi_2 = \rho v_1(a)$ where $v_1(a)$ is the volume of a rod or disk of radius a defined in equation (2.23), and ρ is the density given by N/V where V is the total volume of the unit cell of the finite system. For the 1D systems we take $\phi_2 = 0.35$ and $\phi_1 = 1 - \phi_2 = 0.65$ and for the 2D disks $\phi_2 = 0.25$, and $\phi_1 = 0.75$.

3.2 Calculation of number and volume-fraction variances and excess spreadability

For the 1D systems, we compute $\sigma_N^2(R)$ and $\sigma_V^2(R)$ for the $N = 10^7$ configurations of each chain using 10000 windows randomly distributed in the interval $(R_{\max}, l - R_{\max})$ where R_{\max} is the maximum window radius. The “buffer zone” around the boundaries is to prevent any boundary effects. For the $N = 1.1 \times 10^6$ particles Penrose tiling, the number variance is computed using 100 randomly distributed windows with a maximum radius of $100\rho^{1/2}$. Here the buffer zone was chosen such that at the maximum window radius, the window borders can only be tangential to the cell boundary. To test the theoretical prediction of the α values given by equation (3.9) using $\sigma_N^2(R)$ and $\sigma_V^2(R)$, equation (3.9) is used to find the number $\beta_{N/V}$ such that the scaled number/volume-fraction variance $\sigma_{N/V}^2(R)R^{\beta_{N/V}}$ will have a slope of 0 on a log-log scale (N/V for number and volume respectively). Notice that equations (1.3) and (1.5) suggest that $\beta_{N/V}$ will be the same across all class I systems of the same dimension. To test that the correct $\beta_{N/V}$ were chosen and that the functions $\Lambda_{N/V}(R)$ scale as constants, we calculate the derivative of $\Lambda_{N/V}(R)$ on a log-log scale, i.e., compute

$$\frac{d}{d \log(R)} \log[\Lambda_{N/V}(R)], \quad (3.12)$$

and determine its average, where the average of a function $f(x)$ on the interval $[x_{\min}, x_{\max}]$ is defined as

$$AV[(f(x))] = \frac{1}{x_{\max} - x_{\min}} \int_{x_{\min}}^{x_{\max}} f(x) dx. \quad (3.13)$$

Since these systems possess both microscopic- and “global-scale” oscillations in their number and volume-fraction variances, we refer to intervals containing one peak and one trough of the “global-scale” oscillation as “full effective period”. The interval of integration for averaging is chosen such that it matches as closely as possible an integer multiple of a full effective period.

To compute the spreadability, the structure factor is computed using the scattering intensity function $\mathbb{S}(\mathbf{k})$ and the process described in Section 2 where points of the lattice, \mathbf{r} , are the points at the end of each tile in 1D or the vertices of the Penrose in 2D. In 1D, the reciprocal lattice vectors are then given by

$$\mathbf{k}_n = \frac{2\pi n}{l}, \quad (3.14)$$

where l is the position of the last point in the chain and $n \in \mathbb{Z}$. Notice that increasing l provides higher resolution in \mathbf{k} , and that increasing the number of particles in the chain by a factor of N , results in a decreased size of k_n by a factor of $\approx N$. Since equation (2.15) iterates over each point in the chain and is calculated for each k_n , increasing the particle number of the system by a factor of N results in a N^2 factor increase in computation time for a given k_{\max} . For the Penrose tiling, the structure factor is binned with bins of width $0.01k/\rho$ to find the angular averaged structure factor. Next, since the particles

do not overlap, the spectral density is related to the structure factor via [27, 63, 64]

$$\tilde{\chi}_v(\mathbf{k}) = \phi_2 \tilde{\alpha}_2(k; a) S(\mathbf{k}), \quad (3.15)$$

where a is the radius of the rod/disk. Notice that equation (3.15) implies that the scaling exponent α of $\tilde{\chi}_v(\mathbf{k})$ will be the same as the structure factor $S(\mathbf{k})$. The spectral density is then integrated using equation (2.39) to get the excess spreadability, and the same steps described above for the number and volume-fraction variance are followed while skipping the scaling and running average. Unlike the number and volume-fraction variances, we observe that the excess spreadability of the different systems possesses only “global-scale” oscillations. We therefore average over a time interval that corresponds to a full effective period of this “global-scale” oscillation.

Since α was never calculated for the Penrose tiling and cannot be extracted from the number variance, the function $Z(k)$ is used to extract it by “sandwiching” the function by two curves of the form discussed in Section 2. Since the dimensional dependence of $Z(k)$ is captured by the q^{d-1} term in the integrand, previous work in 1D found scaling of the form $|k|^{1+d}$, but for \mathbb{R}^d , $Z(K)$ will scale like $Z(K) \sim |k|^{\alpha+d}$.

4 Results

4.1 1D chains

4.1.1 Number Variance

In summary, we find that for all the different systems tested, the average values of the derivatives, $\frac{d}{d \log(R)} \log[\Lambda_N(R)]$ (Table 2), all agrees closely (± 0.02) with theoretical predictions of Oğuz et. al [5]. Since some systems described above were not directly investigated by Oğuz et al., our results provide further validity to their theoretical conjecture [equation (3.9) in Ref. [5]]. The local number variances of the Fibonacci, 0112, and 3533 chains, scaled by R^0 since they are class I systems, are shown in Figure 4 as a function of dimensionless window radius $R\rho$, where red lines represent the running average function $\Lambda_N(R)$. Note that despite the Fibonacci and 3533 chains possessing different predicted values of α , this cannot be observed using the number variance, since all class I systems have number variances that asymptotically scale as R^0 . The derivatives of $\Lambda_N(R)$, and their averages indicated by red lines, for all three class I systems are presented in Figure 5. Note that the “global-scale” oscillations in the number variance of the 3533 chain, which will be visible in the volume-fraction variance and the spreadability as well, require a larger interval of integration to capture an integer multiple of full effective period of the “global-scale” oscillations. The near-zero average values of the number variance derivatives (all within ± 0.02) indicate that the asymptotic scaling of the number variances of the different systems is consistent with the theoretical predictions of Oğuz et. al [5] (Table 2 for exact values).

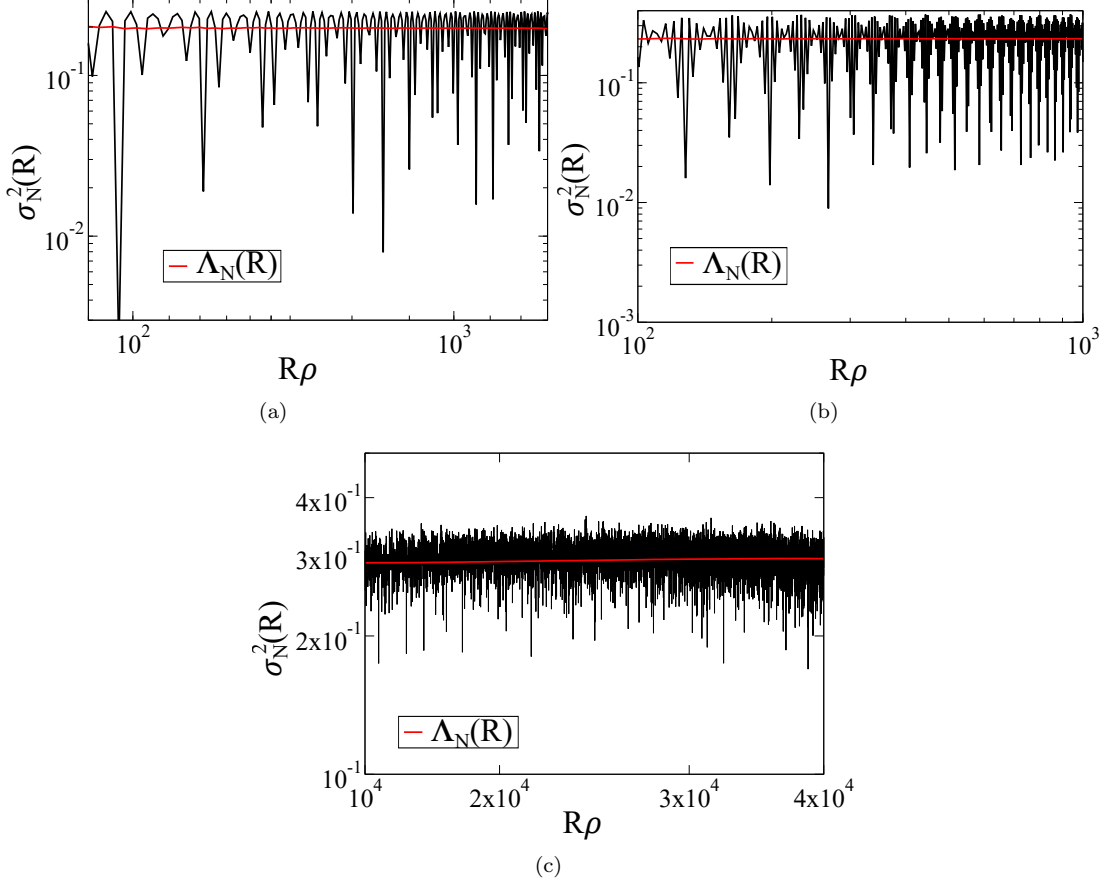


Figure 4: Log-log plots of the local number variances of the class I systems scaled by R^0 with $N = 10^7$ particles as a function of dimensionless window radius $R\rho$, where red lines are the running average functions $\Lambda_N(R)$. (a) Fibonacci chain in the interval $9 \times 10^2 \leq R\rho \leq 4 \times 10^3$. (b) 0112 chain on the interval $10^2 \leq R\rho \leq 10^3$. (c) 3533 chain on the interval $10^4 \leq R\rho \leq 4 \times 10^4$.

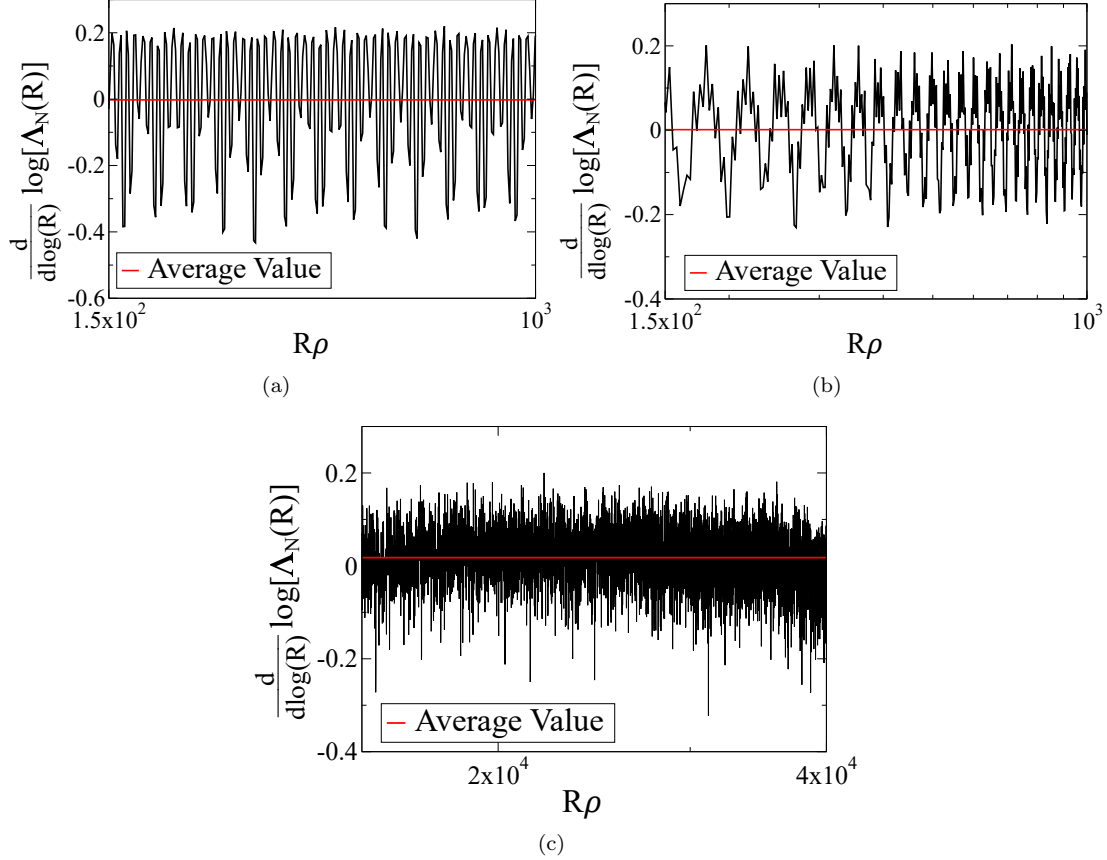


Figure 5: Derivative of the running average function $\Lambda_N(R)$ of the class I systems with $N = 10^7$ particles for large dimensionless window radius $R\rho$. (a) Fibonacci chain in the interval $1.5 \times 10^2 \leq R\rho \leq 10^3$. (b) 0112 chain in the interval $1.5 \times 10^2 \leq R\rho \leq 10^3$. (c) 3533 chain in the interval $10^4 \leq R\rho \leq 4 \times 10^4$.

The scaled number variance of the class II limit-periodic chain and class III 0222 chain are shown in Figure 6(a) and (b) respectively. The number variance scaling factors, $1/\log(R)$ for the limit-periodic and $R^{-0.361}$ correspond to point patterns with $\alpha = 1$ and $\alpha = 0.6390$ scalings. The derivatives $\frac{d}{d\log(R)} \log[\Lambda_N(R)]$, along side their average values indicated by red lines, are shown in Figure 6(c) and (d). Notice that the intervals for integration in Figure 6 were specifically chosen to include an integer multiple of full effective periods of the “global-scale” oscillations .

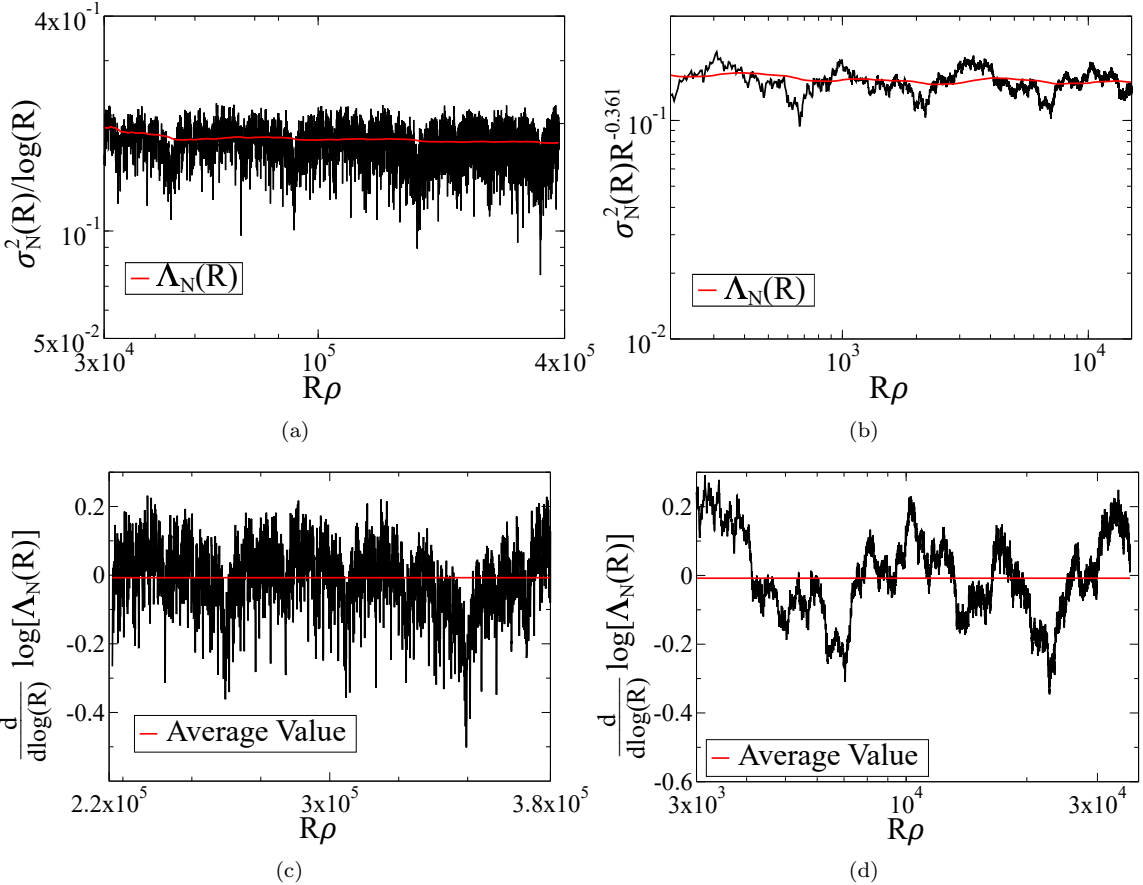


Figure 6: Log-log plots of the scaled local number variances and their derivatives of the class II and III systems as function of dimensionless window radius $R\rho$. (a) Number variance of the limit-periodic chain scaled by $1/\log(R)$, corresponding to $\alpha = 1$, on the interval $3 \times 10^4 \leq R\rho \leq 4 \times 10^5$ and (c) The corresponding derivative of the running average function $\Lambda_N(R)$ over the range $2.2 \times 10^5 \leq R\rho \leq 3.8 \times 10^5$. (b) Number variance of the 0222 chain scaled by $R^{-0.361}$, corresponding to $\alpha = 0.6390$, on the interval $2 \times 10^2 \leq R\rho \leq 2 \times 10^4$. (d) The corresponding derivative of the running average function $\Lambda_N(R)$ over the range $3 \times 10^3 \leq R\rho \leq 4 \times 10^4$.

Figure 7 shows the scaled number variances of the antihyperuniform chains 1530(a) and 0555(b) as a function of dimensionless window radius $R\rho$ in the intervals $5 \times 10^1 \leq R\rho \leq 4 \times 10^4$ and $4 \times 10^1 \leq R\rho \leq 3 \times 10^4$ respectively. The number variances are scaled by $R^{-1.652}$ for the 1530 chain and $R^{-1.0793}$ for the 0555 chain corresponding to their theoretical values of α . It is clear the running average function $\Lambda_N(R)$ smooths out “microscopic-scale” oscillations of the scaled number variance of the 0555 chain (b) which then assists in finding a range that captures a full effective period when averaging the derivative of $\Lambda_N(R)$. Figures 7(c) and (d) present the derivatives of the running average functions $\Lambda_N(R)$ for the two antihyperuniform systems. Notice that the 1530(a) system possesses “global-scale” oscillations in the derivative which make finding a complete effective period to integrate over more difficult, resulting in estimate of the average value of the derivative which is further from 0 than the 0555 chains’ (-0.0081 compared to 0.0027).

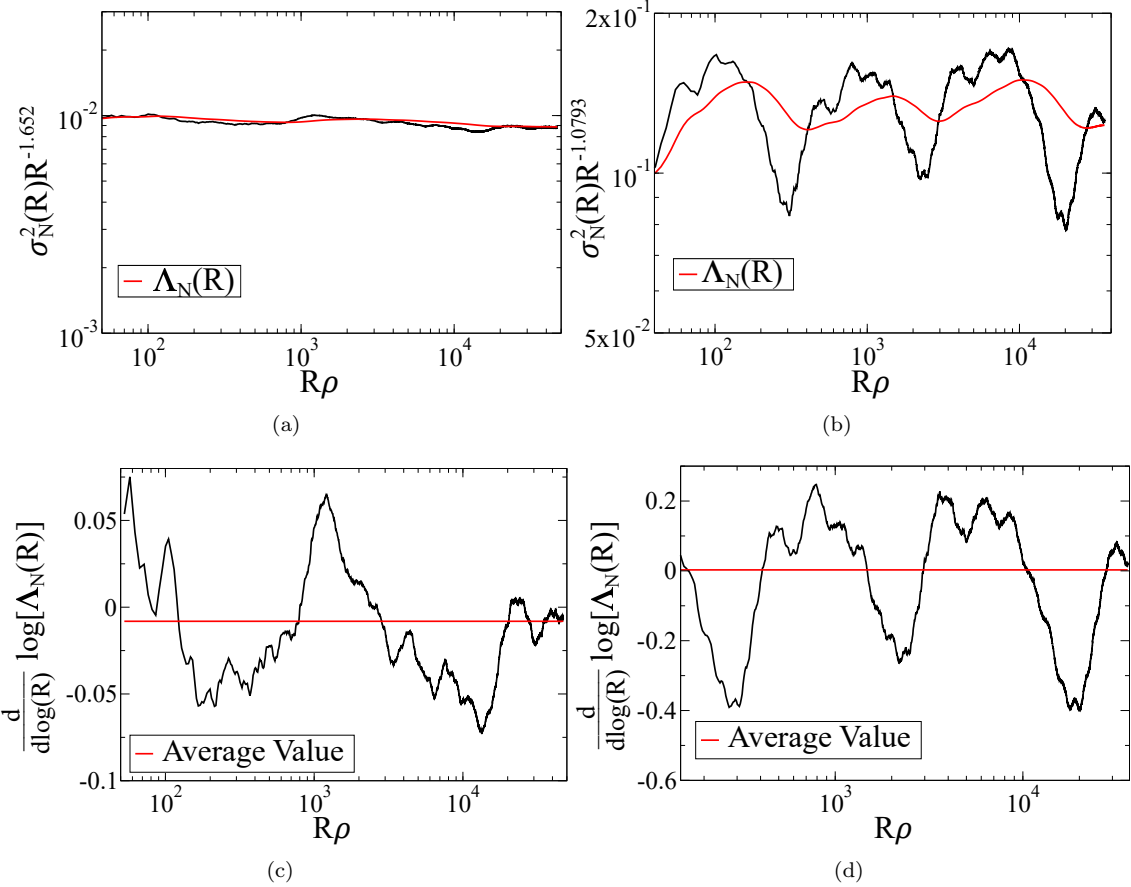


Figure 7: Log-log plots of the scaled local number variances and their derivatives for the antihyperuniform systems with $N = 10^7$ particles as a function of dimensionless window radius $R\rho$. (a) Number variance of the 1530 chain scaled by $R^{-1.652}$, corresponding to $\alpha = -0.652$, on the interval $5 \times 10^2 \leq R\rho \leq 5 \times 10^4$. (c) The corresponding derivative of the running average function $\Lambda_N(R)$ over the range $5 \times 10^2 \leq R\rho \leq 5 \times 10^4$. (b) Number variance of the 0555 chain scaled by $R^{-1.0793}$, corresponding to $\alpha = -0.0793$ on the interval $4 \times 10^2 \leq R\rho \leq 4 \times 10^4$. (d) The corresponding derivative of the running average function $\Lambda_N(R)$ over the range $10^2 \leq R\rho \leq 4 \times 10^4$.

The average values of the derivatives of $\Lambda_N(R)$ for all different 1D systems, as well as the scaling exponents β_N , are shown in Table 2. Notice that all average values are within ± 0.02 of 0, which is a strong indication that the correct scaling exponents were used and that our results are consistent with previous work [5]. The 3533 chain has the largest deviation from the theory, which is attributed here to the “global-scale” oscillations in the number variance, and the difficulty to properly average over a full effective period.

Class	Chain	scaling factor	average value of $\frac{d}{d \log(R)} \log[\Lambda_N(R)]$
I	Fibonacci	R^0	-0.0022
	0112	R^0	0.0013
	3533	R^0	0.0177
II	limit-periodic	$\log(R)^{-1}$	-0.0073
III	0222	$R^{-0.361}$	-0.008
Antihyperuniform	1530	$R^{-1.652}$	-0.0081
	0555	$R^{-1.0793}$	0.0027

Table 2: The average values of the derivative of $\Lambda_N(R)$ for the different systems alongside their scaling exponents

4.1.2 Volume-Fraction Variance

The results reported here are novel since two-phase quasiperiodic systems, such as the ones described in Section 3, have not been characterized and studied before. In summary, we find that for all the different 1D two-phase systems tested, the average values of the derivatives, $\frac{d}{d\log(R)} \log[\Lambda_V(R)]$, are all within ± 0.04 of the theoretical predictions (Table 3), which agrees with our calculation of the number variance (Table 2) as well as theoretical work of Oğuz et. al [5]. Therefore, we show for the first time that a two-phase medium derived from the Fibonacci chain is class I hyperuniform and that the volume-fraction variance can be used to accurately yield values of α for the two-phase substitution tilings described in Section 3. We find that the volume-fraction variance is not superior to the number variance in extracting α from these two-phase tilings (Tables 2 and 3). These results are attributed to the fact that both quantities involve integrals on the spectral density and structure factor respectively, that smooth the spectral functions in similar ways [equations (2.19) and (2.33)]. The local volume-fraction variances of the Fibonacci, 0112, and 3533 chains, scaled by R^2 since they are all class I systems, for dimensionless window radius R/a are shown in Figure 8(a),(b),and (c) respectively, where red lines represent the running average function $\Lambda_V(R)$ and a is the radius of the particles. Note that despite the Fibonacci and 3533 chains possessing different predicted values of α , this cannot be observed using the volume-fraction variance, since all class I systems have volume-fraction variances which asymptotically scale as R^2 , similar to the number variance (cf. Figures 4 and 8). As with the number variance (Figure 5), the “global-scale” oscillations of the 3533 chain require a larger range of R/a to produce a stable average derivative of the volume fraction variance compared to the other class I systems [cf. Figures 9(a) and (b) to (c)]. The derivatives of $\Lambda_V(R)$, and their averages indicated by red lines, for all class I systems are presented in Figure 9. Average values of the derivatives $\frac{d}{d\log(R)} \log[\Lambda_V(R)]$ for all 1D systems are given in Table 2.

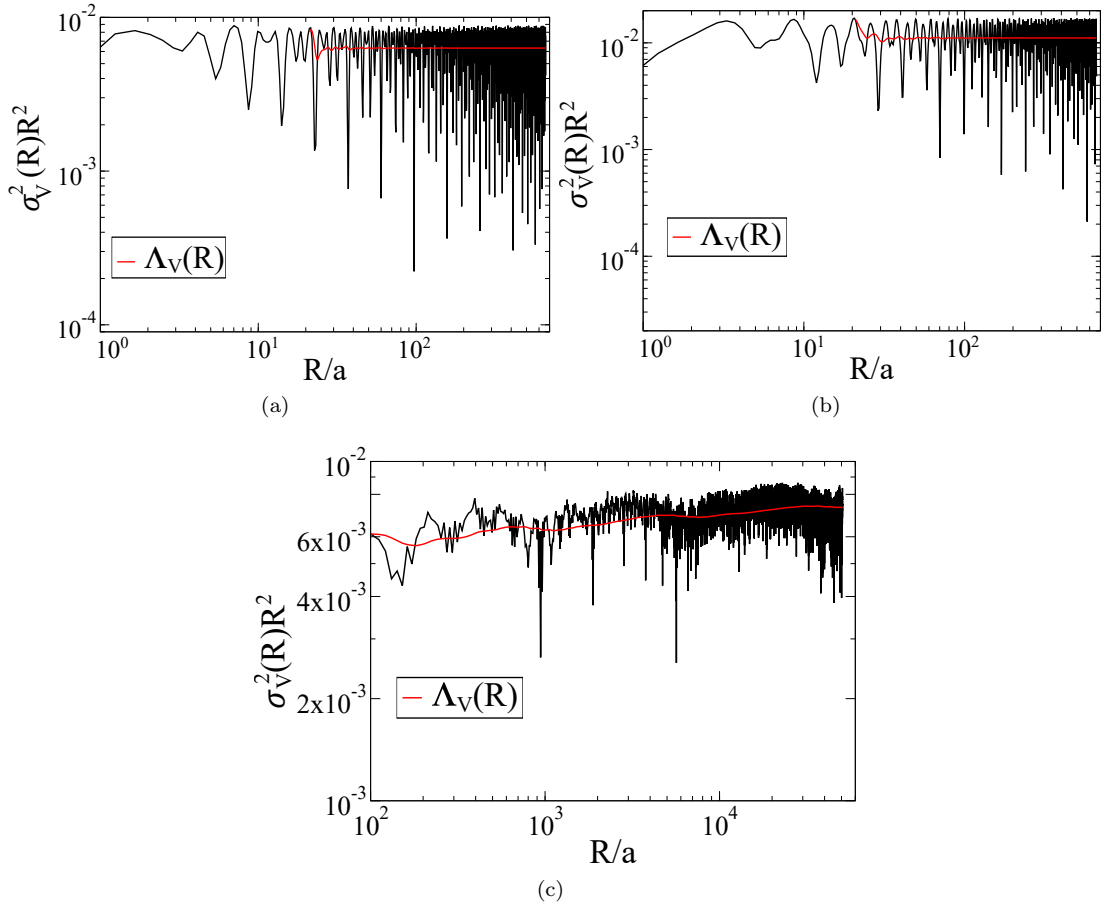


Figure 8: Log-log plots of the volume-fraction variances scaled by R^2 of the class I systems with $N = 10^7$ particles as a function of dimensionless window radius R/a , where a is the radius of the particles with volume fraction $\phi_2 = 0.35$, and red lines indicate the running average functions $\Lambda_V(R)$. (a) Fibonacci chain on the interval $10^0 \leq R/a \leq 7 \times 10^2$ (b) 0112 chain on the interval $10^0 \leq R/a \leq 7 \times 10^2$. (c) 3533 chain on the interval $10^2 \leq R/a \leq 6 \times 10^4$.

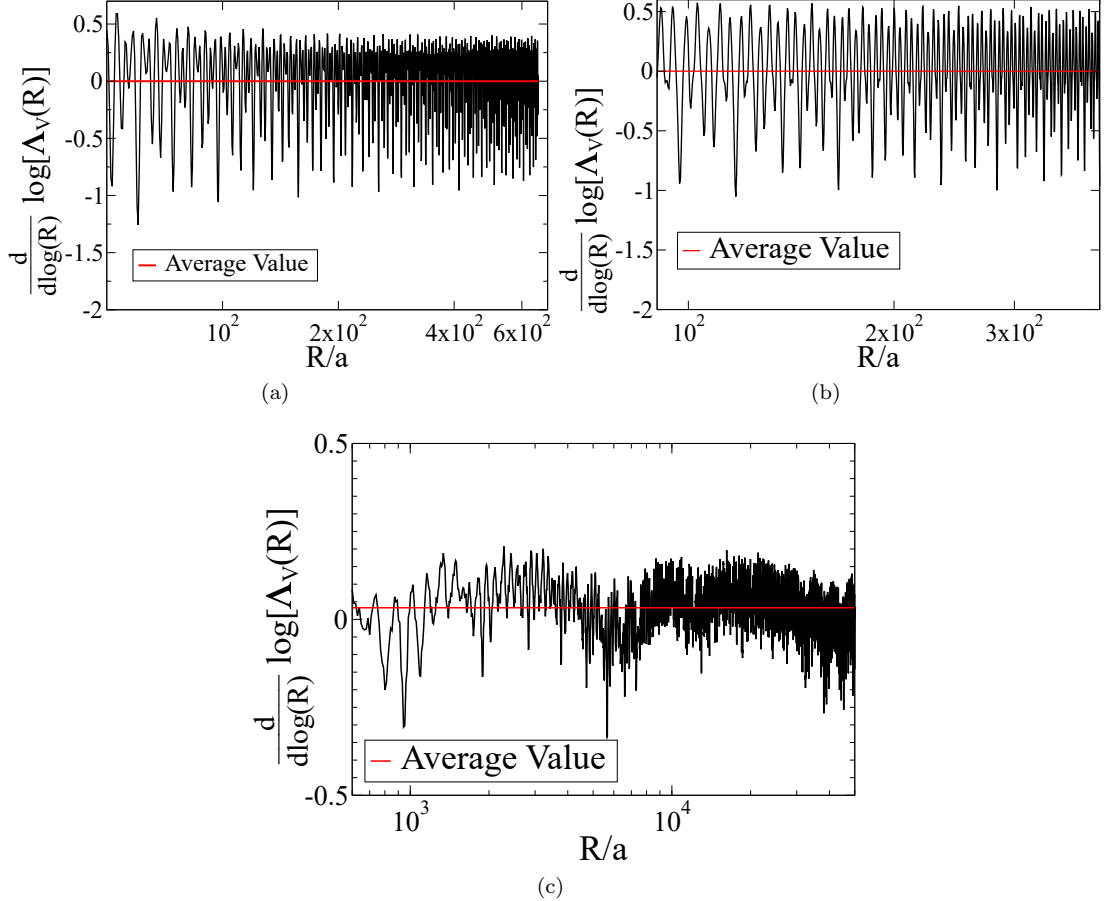


Figure 9: Derivative of the running average function $\Lambda_V(R)$ of the class I systems with $N = 10^7$ particles and volume fraction $\phi_2 = 0.35$ for long dimensionless window radius R/a . (a) Fibonacci chain on the interval $9 \times 10^1 \leq R/a \leq 7 \times 10^2$. (b) 0112 chain on the interval $9 \times 10^1 \leq R/a \leq 4 \times 10^2$. (c) 3533 chain on the interval $6 \times 10^2 \leq R/a \leq 5 \times 10^4$.

The scaled volume-fraction variances of the class II (limit-periodic) and class III (0222) chains are shown in Figure 10(a) and (b) respectively. The volume-fraction variance scaling factors, $R^2/\log(R)$ for the limit-periodic and $R^{1.6390}$ for the 0222 chain correspond to two-phase media with $\alpha = 1$ and $\alpha = 0.6390$ scalings. The derivatives of the running averages, $d/d\log(R) \log[\Lambda_V(R)]$, along with their average values indicated by red lines, are shown in Figures 6(c) and (d), and the integration is taken on the intervals $1.1 \times 10^6 \leq R/a \leq 2.2 \times 10^6$ for the limit-periodic chain, and $10^3 \leq R/a \leq 10^5$ for the 0222 chain. Note that the near-zero average values of the derivatives $d/d\log(R) \log[\Lambda_V(R)]$ (less than ± 0.007) for both systems imply that these two-phase systems are hyperuniform of class II and III with the same values of α as their corresponding point configurations (Section 4.1.1).

Figure 11 shows the scaled volume-fraction variances of the antihyperuniform chains 1530(a) and 0555(b) as a function of dimensionless window radius R/a in the intervals $10^2 \leq R/a \leq 9 \times 10^4$ and $10^1 \leq R/a \leq 6 \times 10^3$ respectively. The volume-fraction variance is scaled by $R^{0.348}$ for the 1530 chain and $R^{0.9207}$ for the 0555 chain corresponding to their respective values of $R^{d+\alpha}$. The derivatives of the running average functions $\Lambda_V(R)$ along side their average values indicated by red lines, are presented in Figures 11(a) and (b) in the intervals $1 \times 10^3 \leq R/a \leq 4 \times 10^4$ and $10^2 \leq R/a \leq 7 \times 10^3$ for the 1530 and 0555 chains, respectively. The near-zero average values of the derivatives $d/d\log(R) \log[\Lambda_V(R)]$ (less than ± 0.02) for both systems imply that these two-phase systems are antihyperuniform with the same values

of α as their corresponding point configurations (Section 4.1.1).

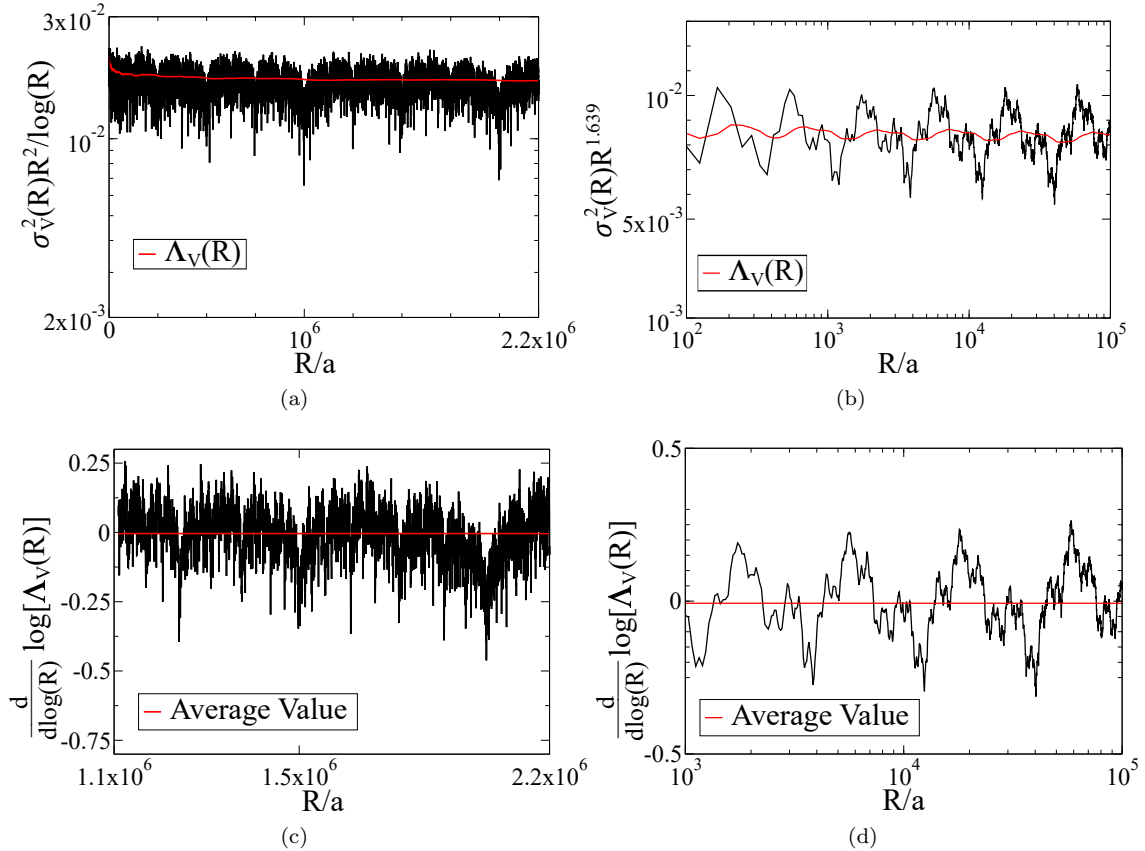


Figure 10: Plots of the scaled volume-fraction variances and their derivatives for the class II and III systems with $N = 10^7$ particles and $\phi_2 = 0.35$ as a function of dimensionless window radius R/a , where a is the radius of the particles. (a) Volume-fraction variance of the limit-periodic chain scaled by $R^2 / \log(R)$, corresponding to $\alpha = 1$ on the interval $0 \leq R/a \leq 2.2 \times 10^6$. (c) The corresponding derivative of the running average function $\Lambda_V(R)$ on the interval $1.1 \times 10^6 \leq R/a \leq 2.2 \times 10^6$. (b) Volume-fraction variance of the 0222 chain scaled by $R^{1.639}$, corresponding to $\alpha = 0.6390$ on the interval $10^2 \leq R/a \leq 10^5$. (d) The corresponding derivative of the running average function $\Lambda_V(R)$ on the interval $10^3 \leq R/a \leq 10^5$.

The average values of the derivatives of $\Lambda_V(R)$ for all different 1D systems are shown in Table 3 as well as the scaling factors R^{β_V} . Notice that all average values are within ± 0.04 of 0, which is a strong indication that the correct scaling exponents were used. The 3533 chain has the largest deviation from the theory (0.03), which is attributed here to the “global-scale” oscillations in the volume-fraction variance, and the difficulty to properly average over a full effective period. These results are further supported by previous work [5], and match with our previous calculations of the number variance (Table 2) as well as with the theoretical equation (3.9).

The results in this section show for the first time that a two phase medium derived from the Fibonacci quasicrystal, is hyperuniform of class I. Moreover, we show that the volume-fraction variance can be used to accurately extract α for 1D two-phase substitution tilings of class II, III and antihyperuniform. Importantly, by comparing our results to sections 4.1.1, we find that the class II, III, and antihyperuniform two-phase systems possess the same values of α as their underlying point patterns. Since equations (2.33) and (2.19) involve integrals on the spectral density and structure factor respectively, that smooth

the spectral functions in similar ways, we find no advantage in using the volume-fraction variance over the number variance in extracting α for the different systems considered. We note that since, by definition, both number variance $\sigma_N^2(R)$, and volume-fraction variance $\sigma_V^2(R)$ do not distinguish values of α of class I systems, we use the spreadability to extract these values from class I systems.

Class	Chain	scaling factor	average value of $\frac{d}{d \log(R)} \log[\Lambda_V(R)]$
I	Fibonacci	R^2	-0.00029
	0112	R^2	0.00024
	3533	R^2	0.03301
II	limit-periodic	$R^2 / \log(R)$	-0.0041
III	0222	$R^{1.639}$	-0.00687
Antihyperuniform	1530	$R^{0.348}$	-0.01924
	0555	$R^{0.9207}$	-0.01284

Table 3: The average values of the derivative of $\Lambda_V(R)$ for the different systems alongside their scaling exponents.

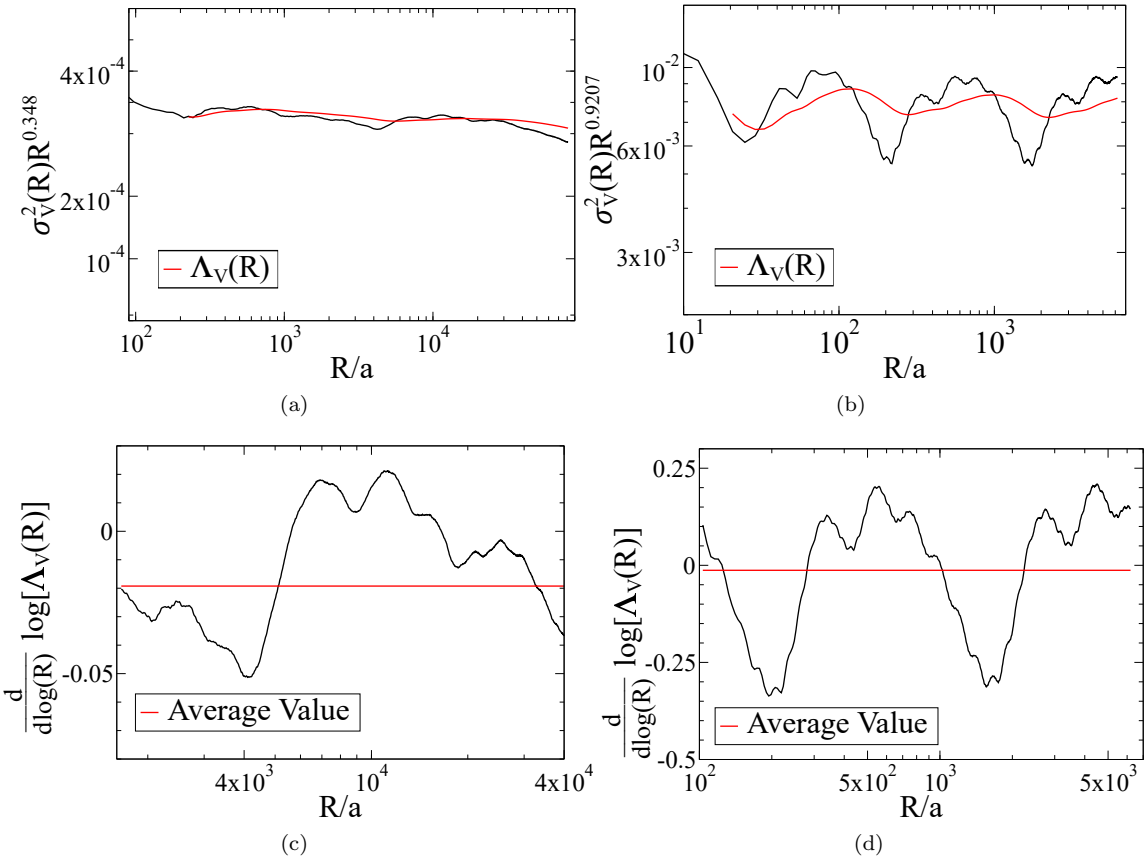


Figure 11: Plots of the scaled volume-fraction variances and their derivatives for the antihyperuniform systems with $N = 10^7$ particles and $\phi_2 = 0.35$ as a function of dimensionless window radius R/a , where a is the radius of the particles. (a) volume-fraction variance of the 1530 chain scaled by $R^{0.348}$, corresponding to $\alpha = -0.652$ on the interval $10^2 \leq R/a \leq 9 \times 10^4$. (c) The corresponding derivative of the running average function $\Lambda_V(R)$ on the interval $10^3 \leq R/a \leq 4 \times 10^4$. (b) Volume-fraction variance of the 0555 chain scaled by $R^{0.9207}$, corresponding to $\alpha = -0.0793$ on the interval $10^1 \leq R/a \leq 7 \times 10^3$. (d) The corresponding derivative of the running average function $\Lambda_V(R)$ on the interval $10^2 \leq R/a \leq 7 \times 10^3$.

4.1.3 Structure Factor

The structure factor of the Fibonacci chain as a function of dimensionless wave number k/ρ in the interval $0 \leq k/\rho \leq 20$ is shown in Figure 12. As described in Ref 57, the structure factor of the Fibonacci chain can be viewed as a union of two sets of periodic yet incommensurate peaks which densely fill reciprocal space (Notice in Figure 12 small peaks in $7 \leq k/\rho \leq 12$). Moreover, the height of the peaks increases linearly with the number of particles, which is predicted from the definition of the scattering intensity function $S(\mathbf{k})$ [equation (2.15)]. Figure 13 shows the structure factors on the smaller interval $15 \leq k/\rho \leq 16$. Notice that as we increase N , not only do the peak heights increase, but we also notice the appearance of new peaks and in the thermodynamic limit ($N \rightarrow \infty$), the set of wave numbers k/ρ corresponding to Bragg peaks becomes dense in the reals [57].

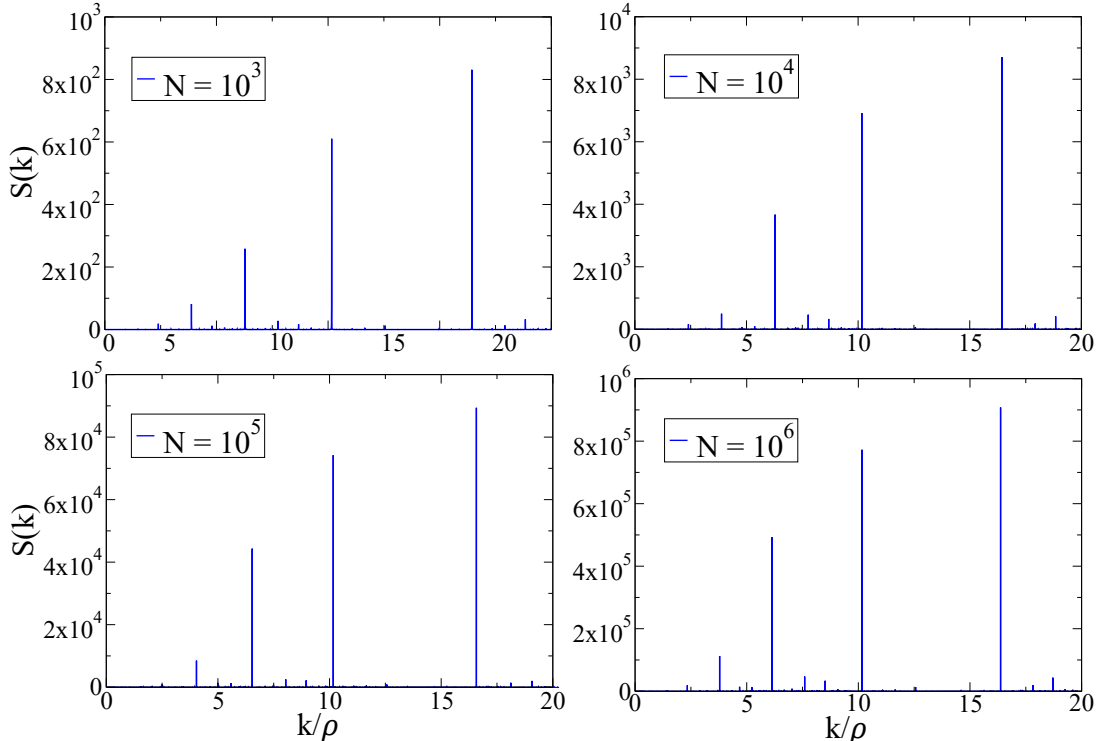


Figure 12: Structure factors of Fibonacci chains with different lengths as a function of dimensionless wave number $0 < k/\rho < 20$. Calculated numerically using the spectral intensity function $S(\mathbf{k})$. Notice the height of peaks increases linearly with chain length.

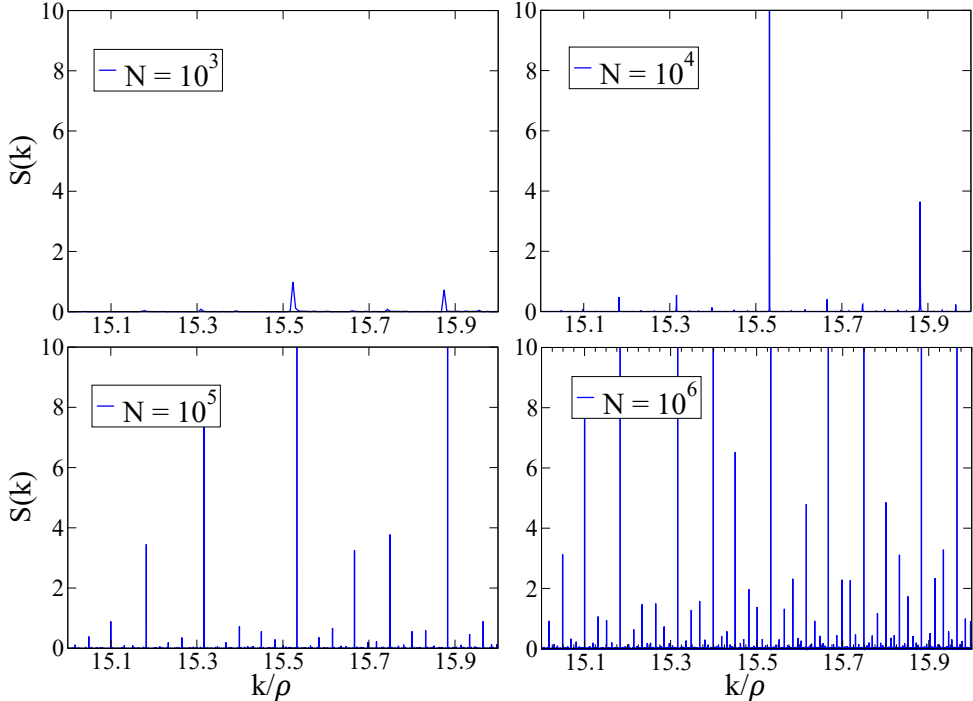


Figure 13: Structure factors of Fibonacci chains with different lengths for a small range of dimensionless wave number $15 < k/\rho < 16$. Calculated numerically using the spectral intensity function $\mathbb{S}(\mathbf{k})$. Notice the formation of new peaks with increasing chain length.

4.1.4 Spreadability

We now use the excess spreadability to extract values of α for all 1D two-phase systems described in Section 3 and compare these values to equation (3.9). Importantly, using the excess spreadability we, expect to distinguish between class I systems which, by definition, cannot be done using the variance calculations. Moreover, as shown in previous work where the spreadability smoothed out numerical noise in spectral densities [23], we expect the spreadability calculations to smooth-out “microscopic-scale” oscillations which were observed in the number and volume-fraction variances. We note that while the integrated intensity function $Z(k)$ is also capable of yielding values of α of any range, including values that correspond to class I systems, the spreadability superior to $Z(k)$, which is characterized by greater uncertainty at small wavenumbers..

In Figure 14 the spreadability of the Fibonacci chain is plotted on a log-log scale against dimensionless time tDs^2 in the interval $5 \times 10^{-2} \leq tDs^2 \leq 10^3$ where $D = 1$ and s is the specific surface given by $s = d\phi_2/a$ for all sphere packing [65]. For all chain lengths $\phi_2 = 0.35$, which then requires $\mathcal{S}(\infty) - \mathcal{S}(0) = \phi_1 = 0.65$. Notice that chains with smaller particle number attain slower-than-expected decay rates at smaller times than the others. Using the mean squared displacement, one can get an estimate of the maximum time t_{\max} attainable given the chain length given by

$$t_{\max} \approx \frac{r_{\max}^2}{2dD} = \frac{2\pi^2}{k_{\min}^2 Dd} \approx \frac{N^2}{2dD}, \quad (4.1)$$

where the last approximation is for the 1D chains only. From the above equation, one might then expect that for the $N = 10^3$ particles chain the maximum time will be $t_{\max} \approx 10^6$ which is clearly not the case seen in Figure 14 where the chain starts to deviate from the rest at around $tDs^2 = 10$. This discrepancy between theoretical and numerical calculations may be due to the density of Bragg peaks in the structure factor of the Fibonacci chain (Section 4.1.3). As discussed above, large time behavior corresponds to the

small k regime, and smallest k values achievable using a finite system of length l are $k_{\min} = 2\pi/l$ and $2k_{\min}$. Thus, compared to infinite systems which have dense Bragg peaks for all k values, we are missing any information contained between our minimal wavenumbers due to finite size effects, and the only way to access it is by using larger systems.

Figure 15 shows the excess spreadability of the different 1D chains, all with $N = 10^7$, as a function of dimensionless time tDs^2 with volume fraction $\phi_2 = 0.35$. Note the different behavior across hyperuniformity classes: all the chains have the same initial value at $t = 0$, since all systems have volume fraction $\phi_2 = 0.35$. Yet, their long time excess spreadabilities are vastly different. The class I systems decay fastest while the antihyperuniform systems flatten quickly which is expected from equation (2.42). Importantly, notice the behavior of the different class I chains: unlike with the number and volume variances, the spreadability of all three class I systems asymptotically scales differently which allows for the extraction of α directly, and not just a confirmation that these are class I systems. Note as well that the intermediate time behavior (around $10^{-1} \leq tDs^2 \leq 10^0$), of the 1530 chain, suggests that on intermediate-length scales the system is very ordered, since its excess spreadability decays exponentially, while at long times it flattens - corresponding to “highly” disordered systems. This difference in order across length scales does not occur in the other systems. While there is much information contained in the short- and long-time behavior of the excess spreadability of these two-phase systems, we leave this for future work. Moreover, notice the oscillations in the excess spreadability of the different systems. These oscillations have not been seen in any other system to date [22–25]. All the different systems posses oscillations in their excess spreadability, the scale of which, both in amplitude and wavelength, are correlated with the oscillations in the number and volume-fraction variances i.e, systems with longer wavelength and larger amplitude oscillations in $\sigma_N^2(R)$ and $\sigma_V^2(R)$ posses excess spreadabilities with oscillations of longer wavelength and larger amplitude. We attribute these oscillations in the spreadability to the behavior of the spectral densities near the origin. As seen in previous work [4], the integrated intensity function $Z(k)$ of the Fibonacci chain possesses a staircase-like shape. We expect this shape to translate to oscillations in the spreadability.

Figure 16 shows the excess spreadabilities of the Fibonacci and limit periodic chains alongside those of known results for other models [22], including the stealthy integer lattice, nonhyperuniform ($\alpha = 0$) Debye random media, and a disordered hyperuniform material (Disordered hyp. in the plot), all with $\phi_2 = 0.35$. Notice that there is a clear distinction between the short- and intermediate-time behavior of the spreadability for the different systems, corresponding to small- and intermediate-length scales. For short times, Torquato [22] showed that the first few terms in the asymptotic expansion of $\mathcal{S}(t)$ are given by:

$$\mathcal{S}(t) = \frac{s}{\phi_2} \left(\frac{Dt}{\pi} \right)^{1/2} - \frac{2ds_2}{\phi_2} (Dt) + \mathcal{O}(Dt/a^2)^{3/2}, \quad (4.2)$$

where s_2 is the second order derivative of $\chi(\mathbf{r})$ at the origin. Indeed, we see that at short times ($10^{-2} \leq tDs^2 \leq 10^{-1}$), all different systems scale similarly due to their identical specific surfaces s . Namely, at $t = 0$, the excess spreadability of all different systems approaches the theoretical value $\phi_1 = 0.65$. The presence of the s_2 term helps distinguish the spreadabilities on a longer time scale, for example the positive value of s_2 for Debye random media contributes to its slower spreadability decay compared to the packings for which $s_2 = 0$ [23]. On long-time scales ($10^{-1} < tDs^2$), the spreadability clearly distinguishes between the different systems. Torquato [22] showed that the spreadability of the

nonhyperuniform Debye media scales as

$$\mathcal{S}(\infty) - \mathcal{S}(t) \sim \frac{(d-1)!d\omega_d\phi_2}{(4\pi Dt/a^2)^{d/2}} - \frac{(d+1)!d\omega_d\phi_2}{(4\pi Dt/a^2)^{(d+2)/2}}, \quad (4.3)$$

which implies asymptotic scaling of $t^{1/2}$. For the disordered hyperuniform medium, Torquato [22] found the scaling

$$\mathcal{S}(\infty) - \mathcal{S}(t) \sim \frac{\phi_1}{4\pi^{1/2}(Dt/a)^{3/2}} - \frac{(d+1)!d\omega_d\phi_2}{(4\pi Dt/a^2)^{(d+2)/2}}. \quad (4.4)$$

For the stealthy integer lattice, Torquato found that the scaling is exponential in time [22]. Equation (2.42) implies the long-time behavior of t^{-2} and t^{-1} for $\alpha = 3$ and $\alpha = 1$ of the Fibonacci and limit-periodic chains, respectively. Notice in Figure 16, the long-time slopes of the excess spreadability are arranged according to the degree of order at large length scales of the corresponding systems. The fastest decay of the spreadability ($\sim e^{-t}$) occurs for a two phase medium derived from the integer lattice, which is the most ordered system of the plot. The slowest decay ($\sim t^{-1/2}$) occurs for the Debye random medium, which is the most disordered system at large length scales. Between the two, the Fibonacci decays with $\sim t^{-2}$, the limit periodic with $\sim t^{-1}$, and the disordered hyperuniform medium, with $\sim t^{-3/2}$. This shows that unlike other quantities, such as the number or volume-fraction variances, the spreadability can be used to characterize accurately the structure of heterogeneous media across all length scales.

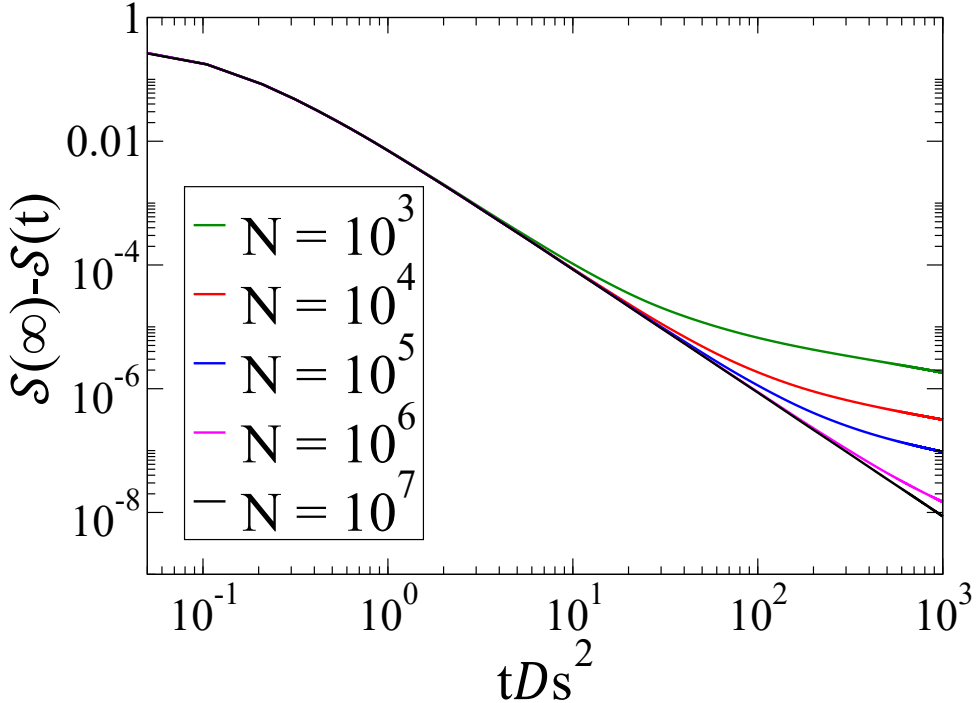


Figure 14: Log-log plot of the excess spreadability for dimensionless time $5 \times 10^{-2} \leq tDs^2 \leq 10^3$ of the Fibonacci chain of different lengths.

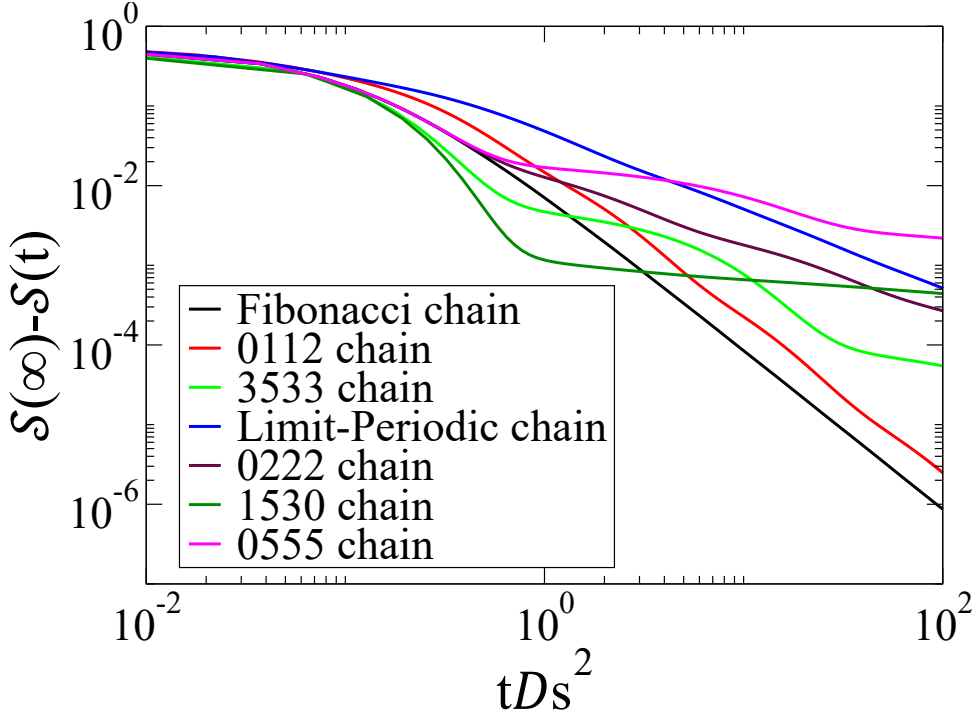


Figure 15: Log-log plot of the excess spreadability for dimensionless time $10^{-2} \leq tDs^2 \leq 10^2$ of the different 1D chains with $\phi_2 = 0.35$. Notice the visible difference between hyperuniformity classes, and even between chains within the same class (Fibonacci,0112,3533 and 1530,0555).

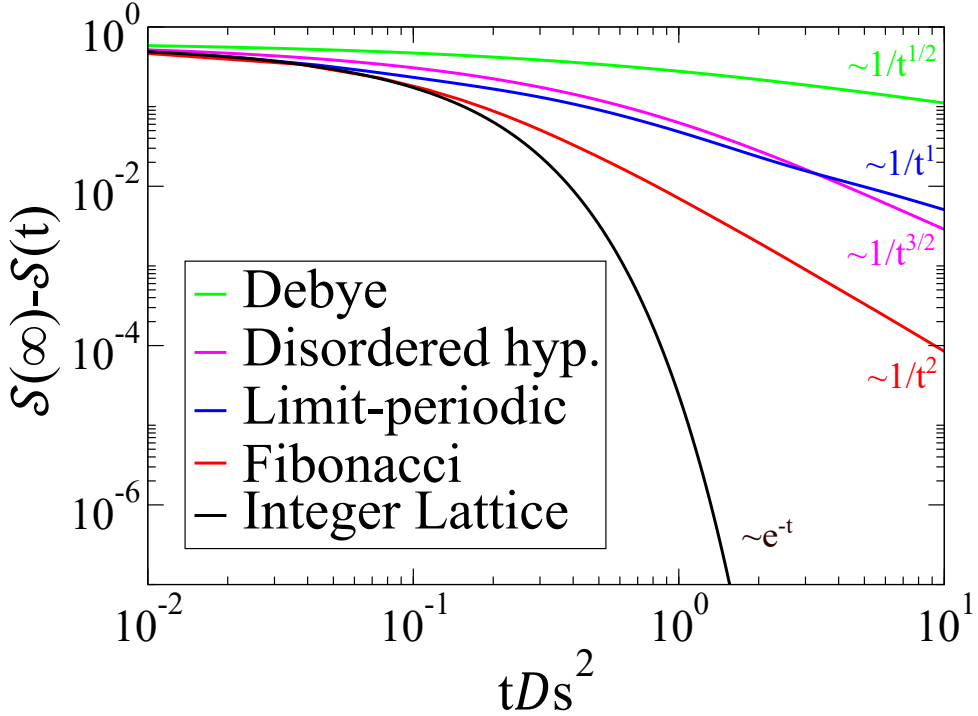


Figure 16: Log-log plot of the excess spreadability for dimensionless time $10^{-2} \leq tDs^2 \leq 10^1$ of different 1D systems with $\phi_2 = 0.35$. The long-time behavior of the spreadability is determined by the degree of large-scale order of the systems where the fastest decay ($\sim e^{-t}$) is for the integer lattice, which is the most ordered system, and the slowest ($\sim t^{-1/2}$) is for the Debye, which is the most disordered at large length scales. The rest of the systems fall between the two. Debye, disordered hyperuniform, and integer lattice taken from [22].

4.1.5 Logarithmic Derivative of the Excess Spreadability

Note that equation (2.42) implies that on a log-log scale, the long-time excess spreadability of the different systems will possess different slopes related to their values of α , namely, the slope will be of the form $-(d + \alpha)/2$. We therefore take a logarithmic derivative of the excess spreadability, $\frac{d}{d\log(t)} \log[\mathcal{S}(\infty) - \mathcal{S}(t)]$, to find the slope and extract α . The logarithmic derivative of the spreadability and its average value indicated by the red line, of the Fibonacci chain with $N = 10^7$ particles as a function of dimensionless time tDs^2 is shown in Figure 17. Notice that compared to the number and volume-fraction variance derivatives, the derivative of the spreadability is much smoother [cf. Figures 17, 5(a), and 9(a)]. This smoothness makes it significantly easier to find and subsequently integrate over a full effective period. The value of α predicted for the Fibonacci chain from equation (3.9) is $\alpha = 3$, which corresponds to large time behavior of t^{-2} in the excess spreadability. This is consistent with the result in Fig. 17 to within $\pm 0.1\%$, thus, we find we can exactly determine α directly from the spreadability, even for class I systems. The logarithmic derivative of the spreadability for the 0112 and 3533 class I chains are presented in Figure 18. The average values are clearly distinguishable from one another, and are within 0.1% of theoretical results (Table 4). Note here, as with the Fibonacci chain, the spreadabilities are significantly smoother than the number and volume-fraction variances. Moreover, notice the comparatively large oscillations in the excess spreadability of the 3533 chain compared to the other class I systems. Larger scale oscillations of similar kind were also observed in the number and volume-fraction variances [Figures 9(c) and 5(c)]. Yet, while the number and volume-fraction variance calculations found that the 3533 was at least one order of magnitude further from the theoretical results than other class I systems (Tables 2 and 3), the spreadability calculation found no difference in accuracy (all class I systems are within 0.1% of theory, Table 4). Therefore, the spreadability oscillations do not significantly impact the result compared to the other class I chains, since they are smoothed out by the Gaussian kernel in the spreadability integral [equation (2.39)].

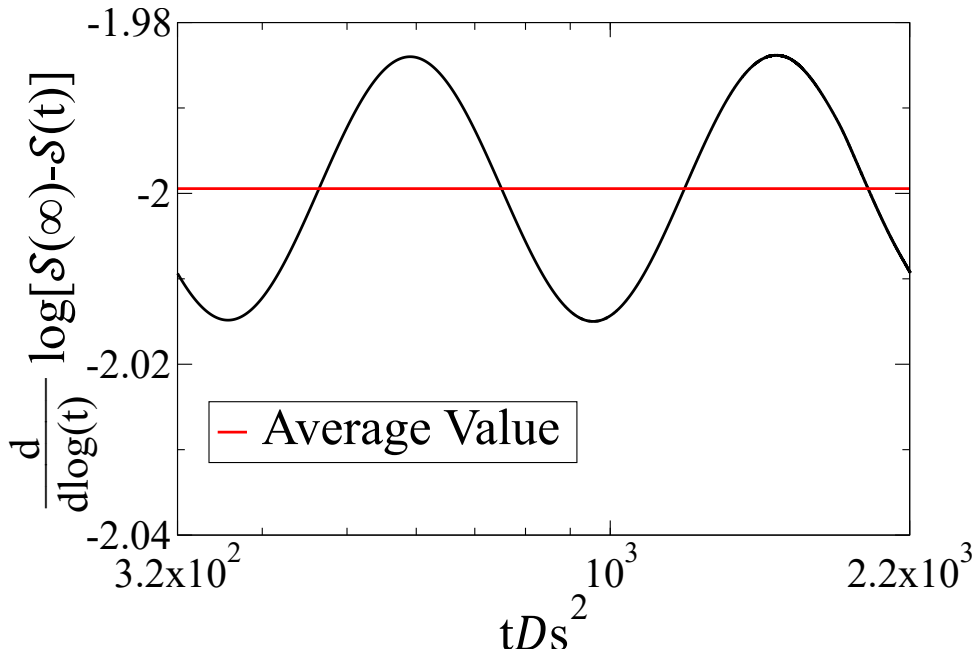


Figure 17: Derivative of excess spreadability of the Fibonacci chain with $N = 10^7$ particles and volume fraction $\phi_2 = 0.35$ for long dimensionless time ($3.2 \times 10^2 \leq tDs^2 \leq 2.2 \times 10^3$).

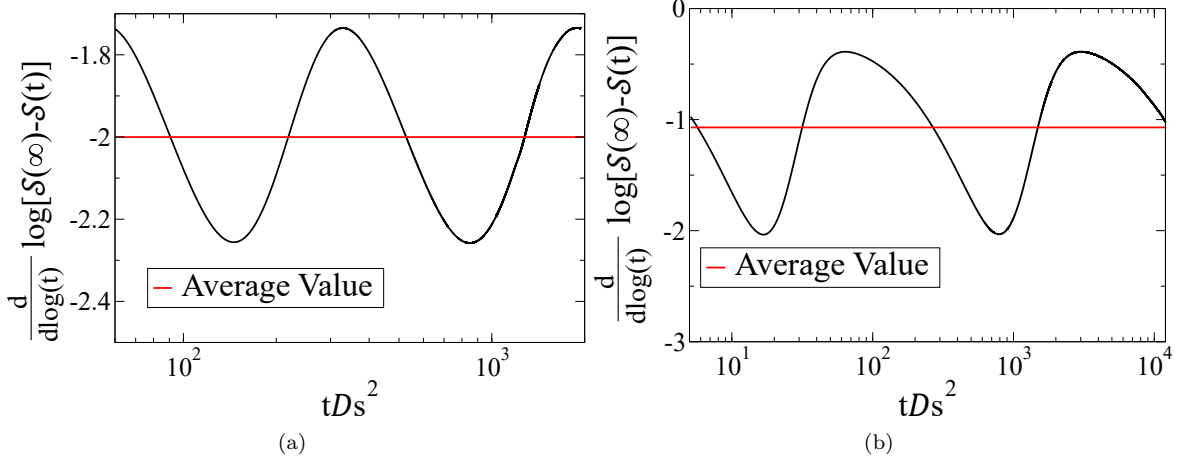


Figure 18: Derivatives of the excess spreadability of the class I systems with $N = 10^7$ and $\phi_2 = 0.25$ as a function of dimensionless time tDs^2 for (a) the 0112 chain over the interval $(6 \times 10^1 \leq tDs^2 \leq 2 \times 10^3)$, and (b) the 3533 chain over the interval $(5 \times 10^0 \leq tDs^2 \leq 10^4)$.

Figure 19 shows the derivative of the excess spreadability for the class II limit-periodic(a) chain as well as the class III 0222(b) chain as a function of dimensionless time tDs^2 . Figure 20 shows the derivative of the excess spreadability as a function of dimensionless time tDs^2 for the antihyperuniform systems. The average values of the derivatives $\frac{d}{d\log(t)} \log[S(\infty) - S(t)]$ of each 1D system, alongside the corresponding value of α calculated from equation (2.42), are presented in Table 4. We note that all the values of α of the class I systems as well as the class III system are within 0.1% of the theoretical result, and for the antihyperuniform systems, the computations were within 0.4%, showing that the spreadability is a powerful tool for accurate extraction of the exponent α with no knowledge of how the system was produced. Moreover, observe that systems that matched best with the theoretical results show “convenient”, almost sinusoidal oscillations in their excess spreadability, compared to systems for which the extracted α was not as accurate (compare Figures 20 (a) and 18 (a) of the 1530 and 0112 chains for example). We believe the results are less accurate for the class II limit periodic chain, since it is shorter, $N \approx 0.6 \times 10^7$ particles, and as discussed at the beginning of this section, shorter chains will flatten faster corresponding to an underestimated value of α , which is observed here. We note that unlike $\sigma_N^2(R)$, and $\sigma_V^2(R)$ that, by definition, cannot distinguish between asymptotic scaling of class I systems, the excess spreadability yields α directly with high accuracy for any system. Notably, the spreadability distinguishes between class I systems, and provides results with high precision (almost all within $\pm 0.5\%$) for all systems of any hyperuniformity class. We note that while the integrated intensity function $Z(k)$, can also yield values of α of any range, including values that correspond to class I systems, the spreadability superior to $Z(k)$, which is characterized by greater uncertainty at small values of k . Second, there was no need of an a priori knowledge of the system’s α to determine it using the spreadability whereas the scaling step of the number and volume-fraction variances, required prior knowledge of α . Third, the excess spreadability smooths-out smaller scale oscillations and produces smoother curves, unlike the number and volume-fraction variances.

Class	Chain	Average derivative value	α	% deviation from theory
I	Fibonacci	-1.9994	2.9988	< 0.1
	0112	-2.0001	3.0002	< 0.1
	3533	-1.0705	-1.141	< 0.1
II	limit-periodic	-0.98063	0.96126	3.874
III	0222	-0.81951	0.63902	< 0.1
Antihyperuniform	1530	-0.17531	-0.64938	0.4
	0555	-0.46051	-0.07898	0.4

Table 4: The average values of the excess spreadability derivatives for the different systems alongside their corresponding hyperuniformity scaling exponent α and the deviation from theory

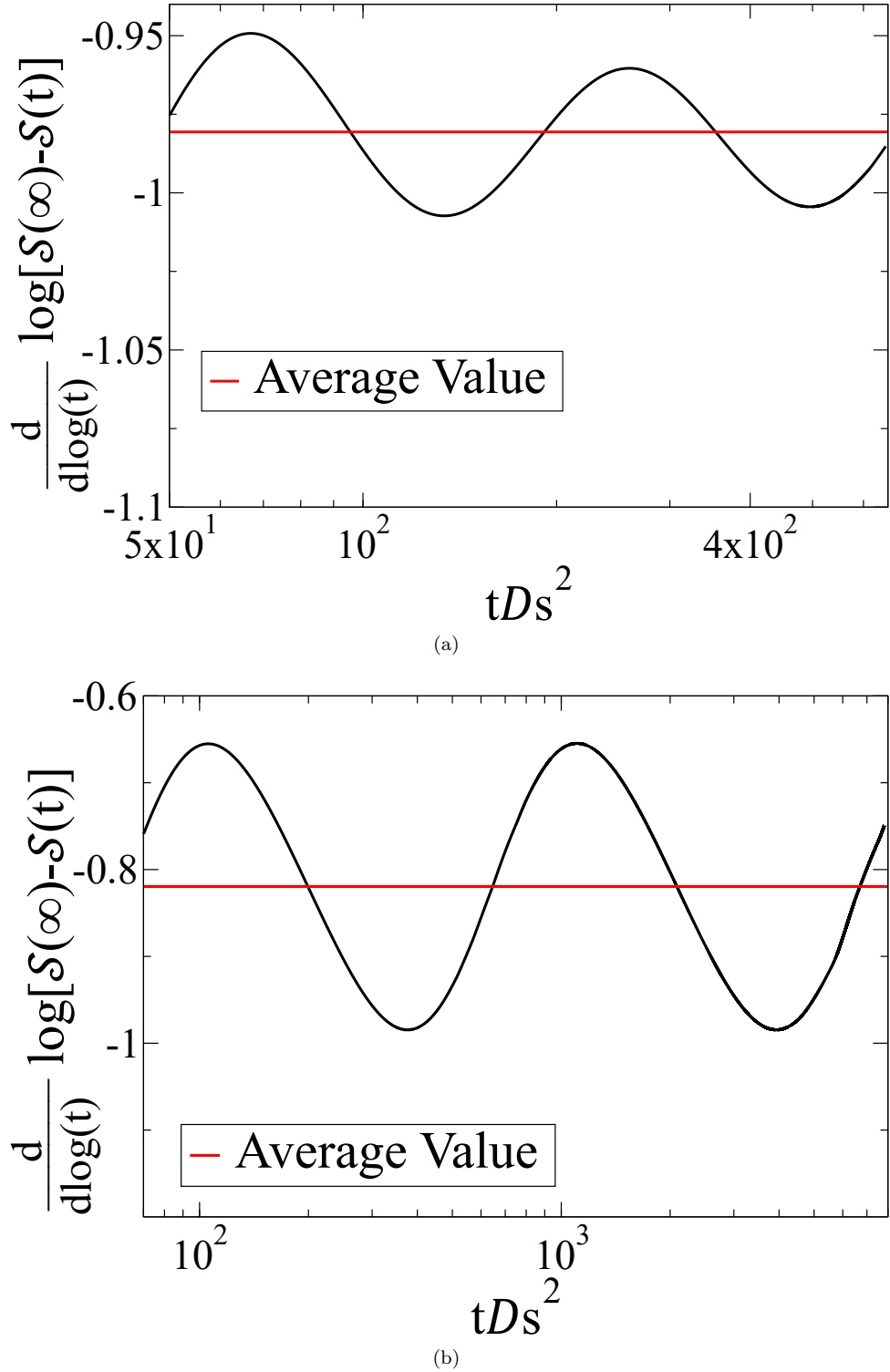
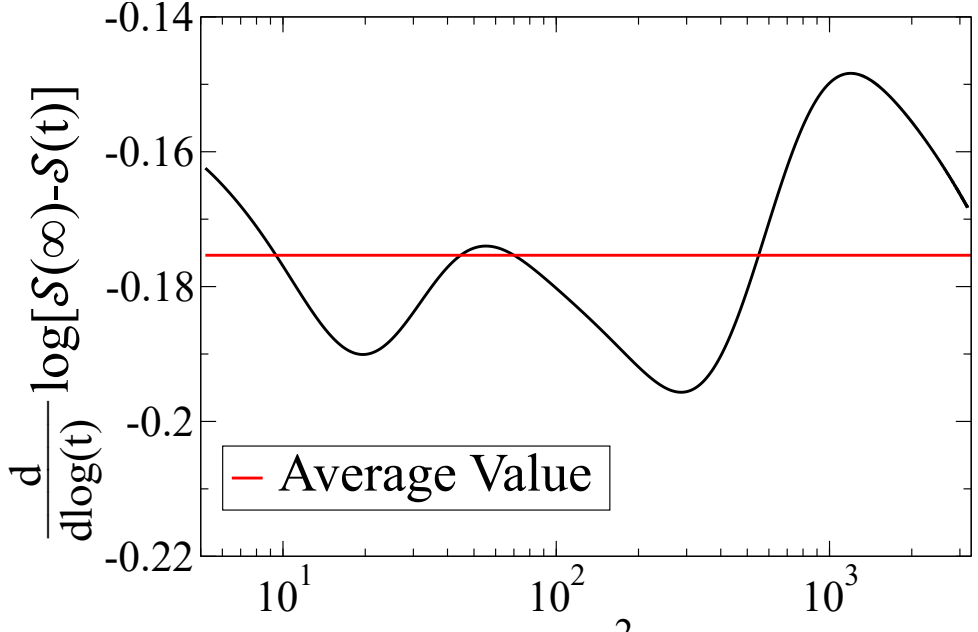
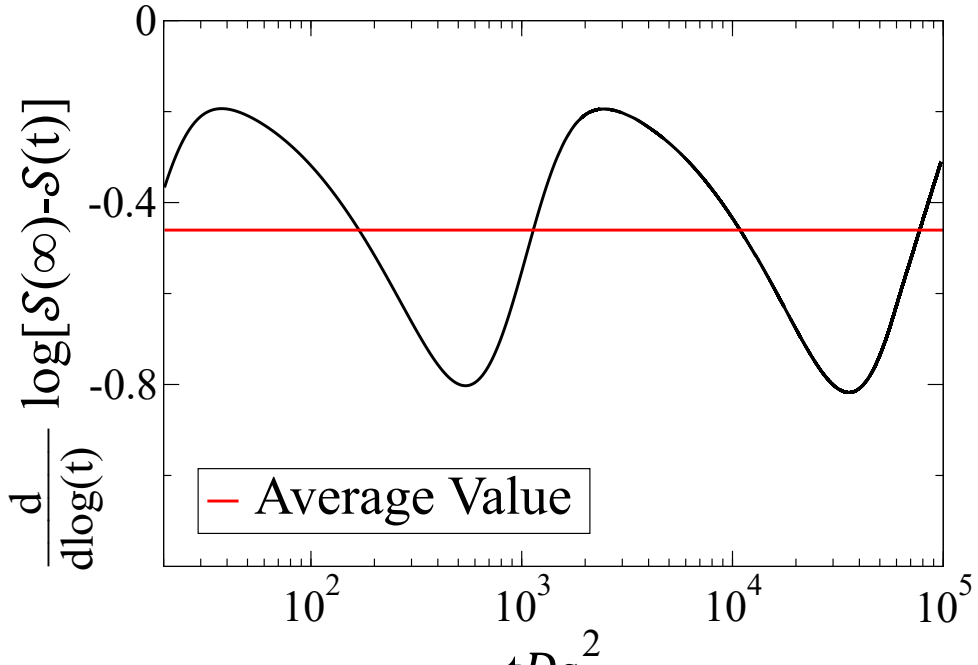


Figure 19: Derivatives of the excess spreadability of the class II and III systems with $N = 0.6 \times 10^6$ and $N = 10^7$ respectively and $\phi_2 = 0.25$ as a function of dimensionless time tDs^2 for (a) the limit-periodic chain on the interval $(5 \times 10^1 \leq tDs^2 \leq 7 \times 10^2)$ and, (b) the 0222 chain on the interval $(7 \times 10^2 \leq tDs^2 \leq 8 \times 10^3)$.



(a)



(b)

Figure 20: Derivatives of the excess spreadability of the antihyperuniform systems with $N = 10^7$ and $\phi_2 = 0.25$ as a function of dimensionless time tDs^2 for (a) the 1530 chain on the interval ($5 \times 10^0 \leq tDs^2 \leq 3.3 \times 10^3$), and (b) the 0555 chain on the interval ($2 \times 10^1 \leq tDs^2 \leq 10^5$).

In this section we showed that for all hyperuniformity classes, and antihyperuniform 1D systems described in section 3, the asymptotic scaling of the number variance matches with theoretical predictions to within ± 0.02 . We note that no information of how the systems were generated was needed for the number variance calculation. Using the volume-fraction variance we showed for first time that as a two-phase medium, the Fibonacci quasicrystal is hyperuniform of class I. Importantly, we find that the class

II, III, and antihyperuniform two-phase systems possess the same values of α as their underlying point patterns (Tables 2 and 3). We note that values of α extracted using the number and volume-fraction variances performed similarly when compared to theoretical predictions (± 0.02 and ± 0.04 respectively), and that the variances possessed both global- and “microscopic-scale” oscillations. We attribute these results to the similarity between equations (2.19) and (2.33), where both $\sigma_V^2(R)$ and $\sigma_N^2(R)$ involve integrals on the spectral density and structure factor respectively, that smooth the spectral functions in similar ways. We also showed that the excess spreadability is a powerful tool capable of extracting values of α to within 0.4% of theoretical predictions for all but one of the systems considered (within 4%). Moreover, we find that the Gaussian smoothing of the spreadability is more robust against “microscopic-scale” oscillations compared to the smoothing operations of the number and volume-fraction variances. The robustness of the spreadability is attributed to the difference in decay rates of $\tilde{\alpha}_2(\mathbf{k}; \mathbf{R})$ which appears in equations (2.19) and (2.33) of $\sigma_N^2(R)$ and $\sigma_V^2(R)$, respectively, which falls off as an inverse power law of the form $1/k^{d+1}$ [2] at large distances, and of the Gaussian function in equation (2.39) for Fourier representation of the spreadability, which falls off superexponentially fast [22] at large times.

The result of the different decay rates is smoother spreadability curves compared to the variances and better α estimates across all 1D systems tested. Given that we have established the superiority of the spreadability to extract the exponent α for either hyperuniform or nonhyperuniform media, we expect it will be a valuable tool to study the large-scale structural properties of other nontrivial two-phase media. We note that the the excess spreadability can distinguishes between class I systems. And while the function $Z(k)$ is also capable of yielding values of α of any range, including those that correspond to class I systems, we expect the spreadability to be much less variable at large time than $Z(k)$ which contains significant variation at small k [4]. Lastly, note that since the 0112, 3533, and 1530 chains were not numerically inspected by Oğuz et al. [5], our results provide further validation to equation (3.9) derived in the aforementioned Reference.

4.2 2D Penrose tiling

The number variance of the Penrose tiling with $N = 1.1 \times 10^6$ particles is seen in Figure 21 where the red line indicates the running average function $\Lambda_N(R)$. Since this is a class I system, the number variance was scaled by a factor of R^{-1} . The derivative of the running average, $\frac{d}{d\log(R)} \log[\Lambda_N(R)]$, is shown in Figure 22 alongside the average value indicated by a red line. Note that the average value of the derivative is close to 0 (-0.0029), which suggests that the correct scaling exponent was used. Yet, it is not possible to extract α from the number variance for class I hyperuniform systems. Figure 23 shows the binned structure factor $S(|\mathbf{k}|)$ of the Penrose tiling as a function of dimensionless wave number k/ρ for $N = 3.5 \times 10^3, 2.5 \times 10^4, 1.7 \times 10^5$, and $N = 1.1 \times 10^6$ particles. Notice that, the peaks increase with number of particles, and so does their density. Figure 24 shows the structure factor on a smaller scale ($12 \leq k/\rho \leq 12.5$) for the same systems, demonstrating the density of Bragg peaks in the structure factor and the increased resolution.

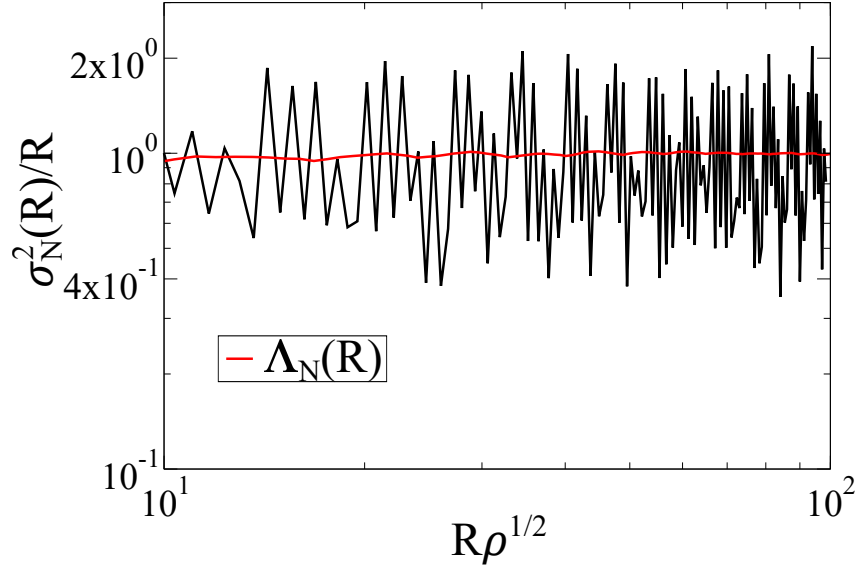


Figure 21: The local number variance of the Penrose tiling with $N = 1.1 \times 10^6$ particles scaled by R^{-1} , corresponding to class I systems in 2D, for dimensionless window radius $10^1 \leq R\rho^{1/2} \leq 10^2$, where the red line is the running average function $\Lambda_N(R)$.

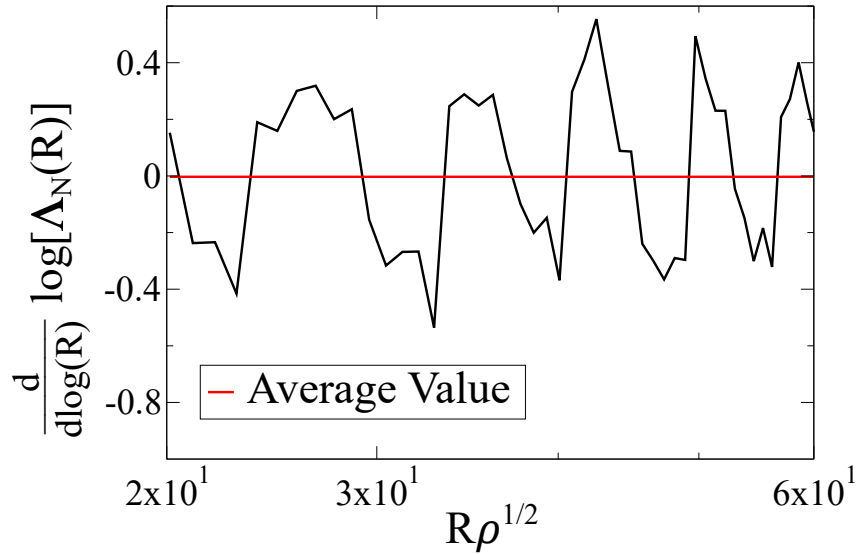


Figure 22: Derivative of the running average function $\Lambda_N(R)$ of the Penrose tiling with $N = 1.1 \times 10^6$ particles at long dimensionless window radius $2 \times 10^1 \leq R\rho \leq 6 \times 10^1$.

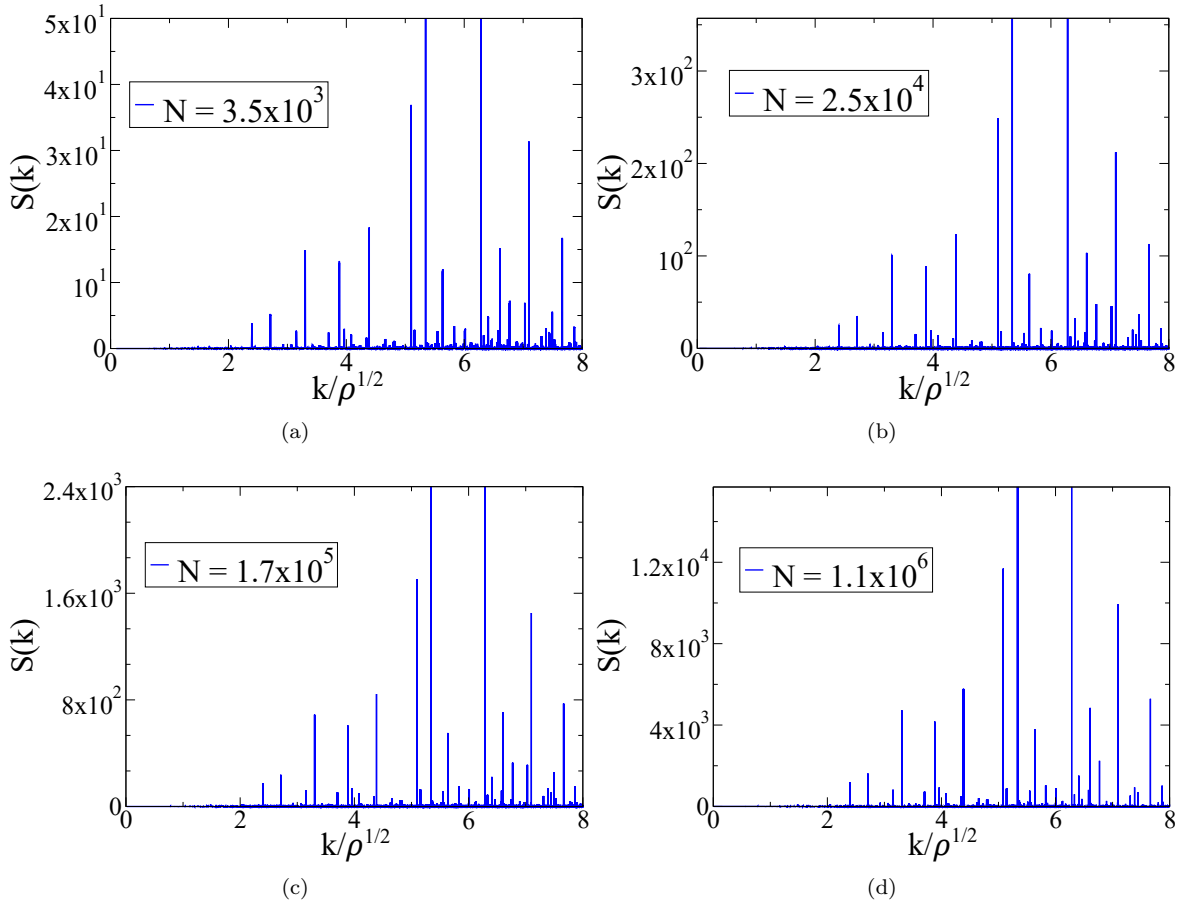


Figure 23: Structure factors for Penrose tilings of different sizes as a function of dimensionless wave number $0 < k/\rho^{1/2} < 8$. Calculated numerically using the spectral intensity function $\mathbb{S}(\mathbf{k})$. Notice the height of peaks increases linearly with chain length.

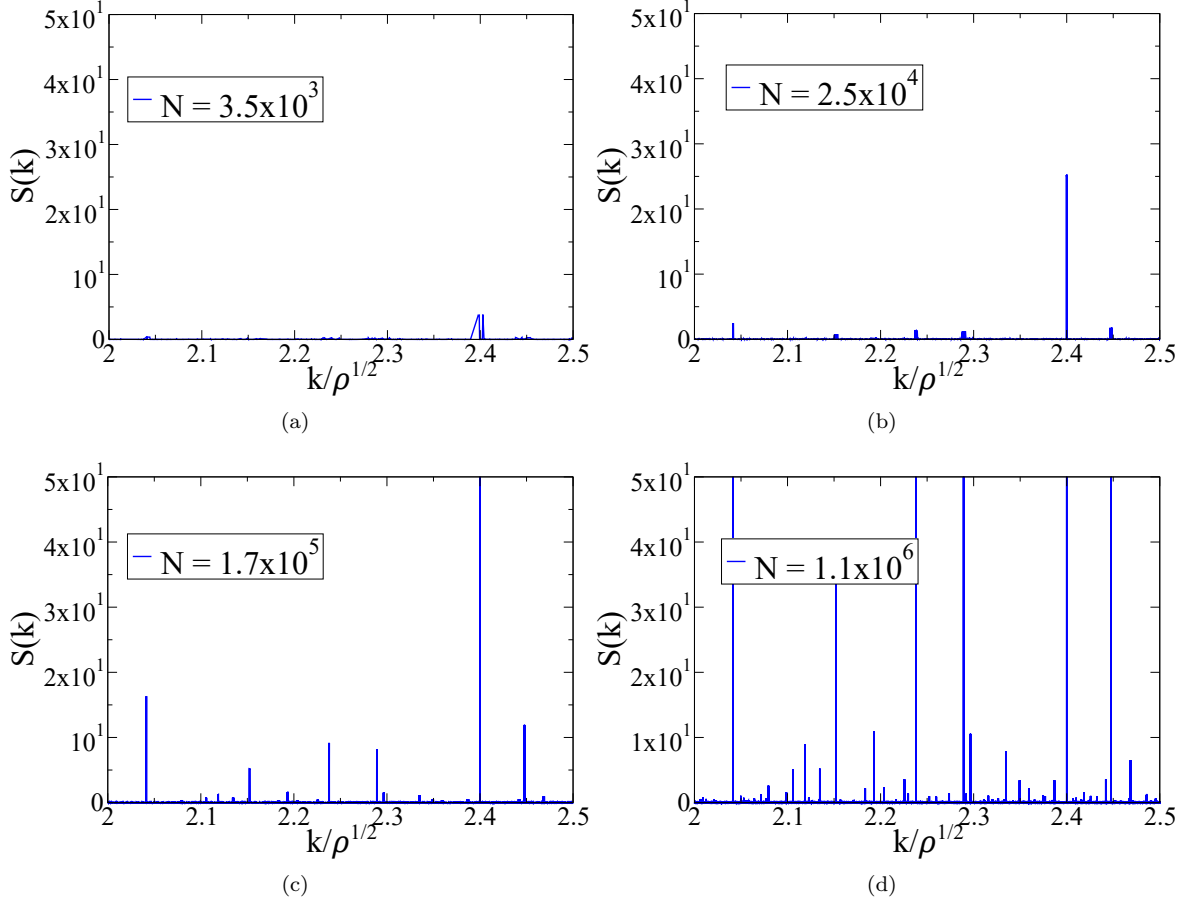


Figure 24: (a) Structure factors of Penrose tiling of different sizes for a small range of dimensionless wave number $2 < k/\rho^{1/2} < 2.5$. Calculated numerically using the spectral intensity function $\mathbb{S}(k)$. Notice the formation of new peaks with increasing chain length.

The excess spreadability as a function of dimensionless time tDs^2 for the Penrose tiling with $N = 3.5 \times 10^3, 2.5 \times 10^4, 1.7 \times 10^5$, and $N = 1.1 \times 10^6$ particles is shown in Figure 25. Notice that again, smaller systems tend to flatten on a shorter scale. The exponential decay that we notice on the $N = 3.5 \times 10^3$ particles system is a numerical effect of all finite systems and was observed for the larger systems as well, but on a longer scale. Note that for short to intermediate time ($10^{-2} \leq tDs^2 \leq 1.1 \times 10^1$) all different systems asymptotically scale similarly, namely, at $t = 0$ all systems are within $\pm 5\%$ of the theoretical value of $1 - \phi_2 = \phi_1 = 0.75$. We observed a high dependency of the initial value $\mathcal{S}(\infty) - \mathcal{S}(0)$ on the binning width of the structure factor. Since the integration in equation (2.39) is over all space and the integrand is always positive, one might expect an underestimation of the excess spreadability for finite numerical evaluations. Yet, we noticed that for bin sizes larger than $0.5k/\rho$, an overestimation of the excess spreadability at $t = 0$ is observed. Since the long-time excess spreadability depends heavily on system size, we conclude that a system size of at least $N = 10^6$ particles be used to extract α . Moreover, we note that unlike the number variance, the excess spreadability curves featured only “global-scale” oscillations. We also suggest that for precise values of the excess spreadability, small bin sizes be used in the structure factor binning procedure.

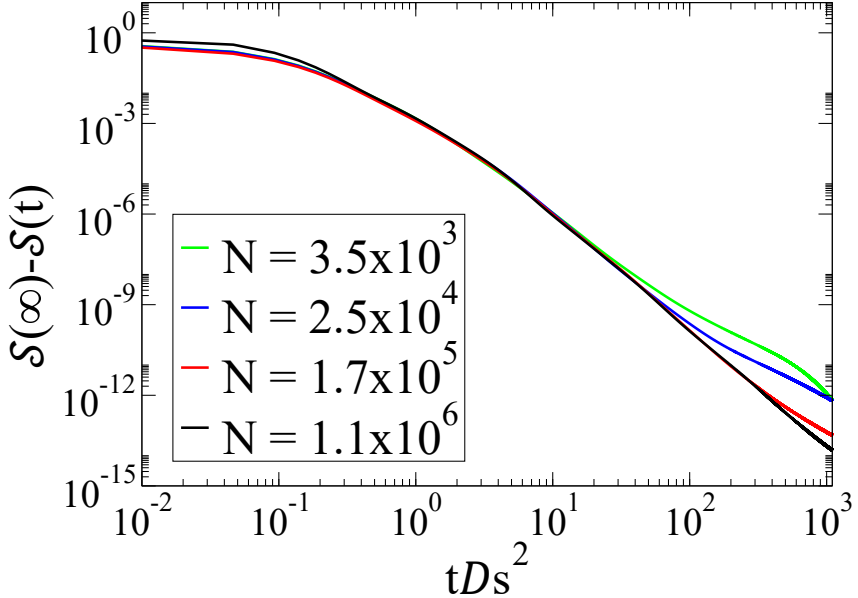


Figure 25: Log-log plots of Spreadabilities of two-phase Penrose tiling with $\phi_2 = 0.25$ for intermediate and large dimensionless times ($0.01 < Dts^2 < 5000$) for different chain lengths. As in the 1D case, notice smaller transfer to exponential decay faster than the large systems.

The derivative of the spreadability of the Penrose tiling, $\frac{d}{d \log(t)} \log[S(\infty) - S(t)]$, with $N = 1.1 \times 10^6$ particles is shown in Figure 26 where the red line indicates the average value. The average value of the derivative is -3.862 which corresponds to $\alpha = 5.724$. Note that this value cannot be extracted from the number variance and it is the first time, as far as we know, this value is reported. The excess spreadability of the $N = 1.1 \times 10^6$ particles Penrose tiling alongside a line with the average value calculated from the derivative is shown in Figure 27. Figure 28 shows a log-log plot of the function $Z(K)$ [equation (2.16)] for the binned structure factor of the Penrose tiling with $N = 1.1 \times 10^6$ particles. Red lines correspond to lines of slope $7.7 = \alpha + 2$. Note that the value of alpha suggested by Figure 28 is $\alpha = 5.7$ which closely matches (within 0.4%) the results from the spreadability. Importantly, the results of the spreadability and $Z(k)$ can be compared here due to the simple nature of equation (3.15). Since $\tilde{\alpha}_2(\mathbf{k}; \mathbf{R})$ only contributes as a coefficient to the spectral density, we expect the structure factor and spectral density to scale similarly in small wave numbers. Moreover, although both $Z(k)$ and the excess spreadability can be used to extract α , $Z(k)$ is simply a choice of a smoothing function and still requires diffraction information, while the spreadability has a physical, measurable effect which can be extracted from both direct and Fourier-space methods.

In this section we showed that the number variance of the Penrose tiling asymptotically scales closely (± 0.003) to that of class I hyperuniform system which agrees with previous results [54]. Using the long-time excess spreadability, we estimate for the first time that the hyperuniformity scaling exponent α of the two-phase medium derived from the Penrose tiling is $\alpha = 5.724$ and using the integrated intensity function $Z(k)$ we found a scaling exponent that matches the spreadability to within 0.4%. We expect the spreadability and $Z(k)$ to agree since for packings, the structure factor and spectral density scale with the same value of α in small wave numbers due to the trivial relation between them [equation (3.15)]. We note that since the number variance by definition cannot be used to extract α from class I systems, one must use a different method, such as the spreadability. Moreover, while the integrated intensity function $Z(k)$, can also yield values of α of any range, including values that correspond to class I systems, the spreadability is superior to $Z(k)$, which is characterized by greater uncertainty at small

wavenumbers. Furthermore, we note that while both the number variance and $Z(k)$ can be regarded as a smoothing operation of the structure factor, we find that the spreadability is more robust against “microscopic-scale” oscillations, resulting in a smoother curve and better α estimates.

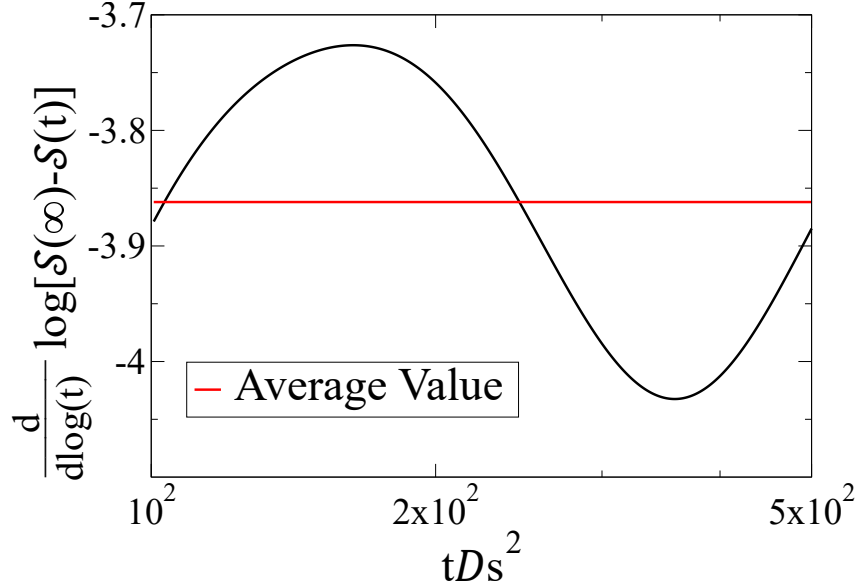


Figure 26: Log-log plot of the derivative of excess spreadability of the Penrose tiling with $N = 1.1 \times 10^6$ particles and volume fraction $\phi_2 = 0.25$ for long dimensionless time ($10^2 \leq tDs^2 \leq 5 \times 10^2$). The average value is -3.862 which corresponds to a value of α of $\alpha = 5.724$.

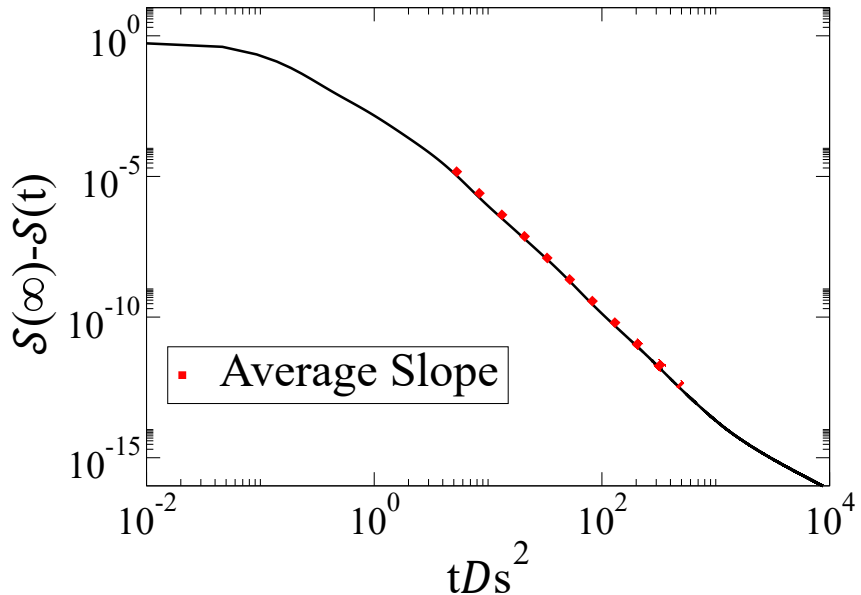


Figure 27: Log-log plot of excess spreadability of the Penrose tiling with $N = 1.1 \times 10^6$ particles and volume fraction $\phi_2 = 0.25$ dimensionless time ($10^{-2} \leq tDs^2 \leq 10^4$). Red line is calculated average slope corresponding to $\alpha = 5.724$.

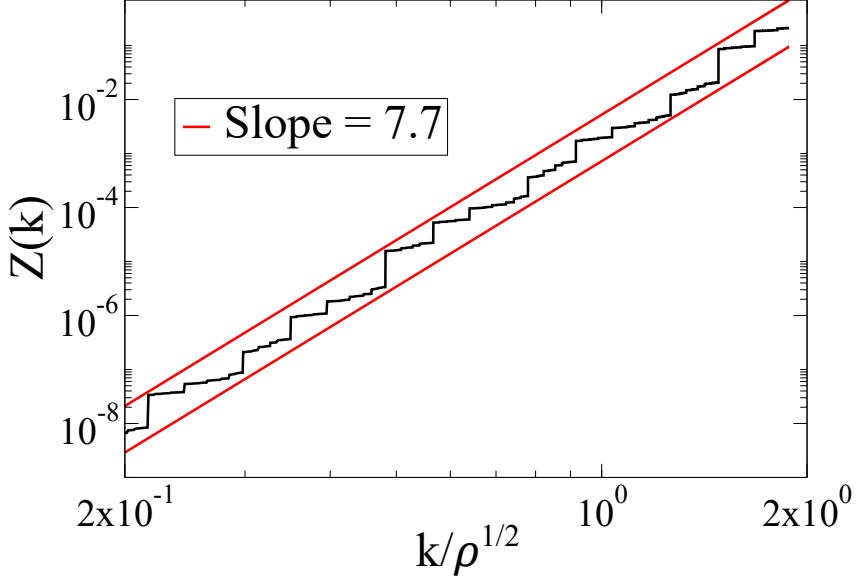


Figure 28: $Z(k)$ for a Penrose tiling computed using the structure factor in Figure 23. Red lines with slope of 7.7 suggest upper and lower bounds. The scaling exponent found is $\alpha = 7.7 - 2 = 5.7$

5 Discussion

In this work, we investigated for the first time the hyperuniformity and time dependent properties of two-phase quasicrystals in one and two dimensions, as well antihyperuniform and hyperuniform one-dimensional substitution tilings of all three hyperuniformity classes. The one-dimensional models consist of the class I Fibonacci chain quasicrystal, 0112 substitution tiling, 3533 substitution tiling; class II limit-periodic substitution tiling; class III 0222 substitution tiling; and the antihyperuniform 1530 and 0555 substitution tilings. The two-dimensional model considered is the Penrose tiling of class I. For the one-dimensional systems, we calculated both the number and volume-fraction variances [$\sigma_N^2(R)$ and $\sigma_V^2(R)$], as well as their excess spreadabilities, $\mathcal{S}(\infty) - \mathcal{S}(t)$, to accurately capture their hyperuniformity scaling exponents α . We also validated previous theoretical predictions to benchmark our numerical calculations. Furthermore, given that we have established that the spreadability can be used to probe with high precision either one- or two-dimensional two-phase media derived from quasicrystals across hyperuniform and nonhyperuniform classes including antihyperuniform, we expect it will be a valuable tool to study the large-scale structural properties of other nontrivial two-phase media. Moreover, we compared our numerical calculations of systems that were not explored numerically to test the validity of theoretical predictions and conjectures on these systems. For the two-dimensional Penrose tiling and packing we calculated the number variance and excess spreadability as well as the integrated intensity function $Z(k)$.

Our calculations of the number variance for the one- and two-dimensional systems (Table 2 and Section 4.2) match theoretical predictions for all systems considered [5, 54]. Since some configurations tested here were never explored numerically, these results provide further validation for equation (3.9) from Ref. [5]. Using the volume-fraction variance we showed for the first time that the two-phase medium derived from the Fibonacci quasicrystal is hyperuniform of class I. Moreover, we find that all 1D two-phase systems considered belonged to the same hyperuniformity class as their underlying point configurations. We also show that Class II, III and antihyperuniform systems possess the same values of α as their corresponding point configurations (Table 3). Thus, the number and volume-fraction variances can be used to accurately extract α from 1D hyperuniform systems of class II, III, and nonhyperuniform class

including antihyperuniform. We find that the volume-fraction variance is not superior to the number variance in extracting α , since both quantities involve integrals on the spectral density and structure factor respectively, that smooth the spectral functions in similar ways. This results in both quantities being susceptible to similar kinds of “microscopic-scale” oscillations.

The excess spreadability calculations showed for the first time that the two-phase medium derived from the Fibonacci chain is hyperuniform with scaling exponent of $\alpha = 3$. Moreover, for all but one of the 1D two-phase systems considered, we found that values of α closely match theoretical values predicted by Oğuz et al. [5] (Table4). This provides a benchmark for the spreadability, to be used on systems who’s values of α we do not yet posses. Moreover, we used the long-time excess spreadability to report for the first time an estimation of $\alpha \approx 5.7$ for the two-phase medium derived from the Penrose tiling. This result is supported by the integrated intensity function $Z(k)$ calculations and its upper and lower bounding functions. We also note that compared to the smoothing operations produced by the integrals in the computation of the functions $\sigma_N^2(R)$, $Z(k)$, and $\sigma_V^2(R)$, the smoothing operation produced by the Gaussian kernel of the spreadability is more robust against “microscopic-scale” oscillations, resulting in smoother curves which allow for an easier selection of averaging interval, and thus, more accurate estimates of α compared to theory. The robustness of the spreadability is attributed to difference in the decay rate of $\tilde{\alpha}_2(\mathbf{k}; \mathbf{R})$ which appears in equations (2.19) and (2.33) of $\sigma_N^2(R)$ and $\sigma_V^2(R)$, respectively, which falls off as an inverse power law of the form $1/k^{d+1}$ [2] at large distances, compared to the decay of the Gaussian function in equation (2.39) for the Fourier representation of the spreadability, which falls off superexponentially fast [22] at large times. We find that the spreadability allows one to accurately distinguish different class I systems, and compute α directly for any hyperuniform or non-hyperuniform classes, including antihyperuniform systems. We note that while the integrated intensity function $Z(k)$, can also yield values of α of any range, including values that correspond to class I systems, the spreadability is superior to $Z(k)$, which is characterized by greater uncertainty at small wavenumbers.

Our results are novel since it is the first time two-phase media derived from quasiperiodic point-patterns are constructed, and their values of α are computed. Moreover, we report remarkable “global-scale” oscillations in the spreadability of the quasiperiodic two-phase media which have not been observed in other systems such as sphere packings derived from uniformly randomized lattices, “perfect glasses”, disordered stealthy hyperuniform point processes, Bravais lattices, superballs, Debye random media, and nonhyperuniform fully penetrable spheres [22–25]. While we computed the values of α of two-phase media derived from quasicrystals, other physical properties of these systems can be explored in future works. Further numerical calculations can be done on other two- and three-dimensional quasicrystals, as well as theoretical work to confirm our numerical estimates, especially for the Penrose tiling since we do not have any other estimates of its value of α . Moreover, for specific configurations of the substitution matrix \mathbf{M} , one finds that $\lambda_2 = 0$, and since it appears inside a logarithm in equation (3.9), one cannot use its predictions to properly extract a value of α (Ref. 5). It is an interesting question how the excess spreadability of such systems will behave. Furthermore, the characterization of the “global-scale” oscillations in the spreadability, and their relation to the microscopic- and “global-scale” oscillations in the number and volume-fraction variances is an avenue for future research.

Acknowledgements

This work would not have been possible without the help of my mentors,cloogues, and friends. For his important comments, amazing commitment and availability, and most of all mentorship and guidance

throughout this project, I thank my advisor Salvatore Torquato. I thank Professor Paul J. Steinhardt for being my second reader. To Charles Maher for producing the Fibonacci chain figure, and for helping me with every step of the way, including reading about 100 drafts of this work. Without him this work would not have been possible. I thank the Torquato group for being extremely warm and welcoming during the long hours in the office. To Aidan Zentner for producing, and allowing me to use, the different configurations considered in this work. Thank you to Rahul Jain for being an amazing roomie and friend, and for taking care of me while I worked into the late hours of the night. To Chirag Kumar for his never ending positive and supportive attitude, and for helping me set up and run jobs on the cluster. To Maryam Kamel for always being supportive of me and everyone around her. To my Family and friends in and outside Princeton. To Domenic Ferreris for always letting me win in pool, for going through this physics journey with me, and for putting up with all of my nonsense. Lastly to Dafna Yavetz for her never-ending support, love, belief in me, and most of all, for making me a better person.

References

- [1] P. M. Chaikin, T. C. Lubensky, and T. A. Witten, *Principles of condensed matter physics*, **10** (1995).
- [2] S. Torquato and F. H. Stillinger, *Local density fluctuations, hyperuniformity, and order metrics*, Physical Review E **68**, 041113 (2003).
- [3] C. E. Zachary and S. Torquato, *Hyperuniformity in point patterns and two-phase random heterogeneous media*, Journal of Statistical Mechanics: Theory and Experiment **2009**, P12015 (2009).
- [4] E. C. Oğuz, J. E. Socolar, P. J. Steinhardt, and S. Torquato, *Hyperuniformity of quasicrystals*, Physical Review B **95**, 054119 (2017).
- [5] E. C. Oğuz, J. E. S. Socolar, P. J. Steinhardt, and S. Torquato, *Hyperuniformity and anti-hyperuniformity in one-dimensional substitution tilings*, Acta Crystallographica Section A **75**, 3 (2019).
- [6] O. U. Uche, S. Torquato, and F. H. Stillinger, *Collective coordinate control of density distributions*, Physical Review E **74**, 031104 (2006).
- [7] O. U. Uche, F. H. Stillinger, and S. Torquato, *Constraints on collective density variables: Two dimensions*, Physical Review E **70**, 046122 (2004).
- [8] A. Gabrielli, M. Joyce, and S. Torquato, *Tilings of space and superhomogeneous point processes*, Physical Review E **77**, 031125 (2008).
- [9] A. Gabrielli, *Point processes and stochastic displacement fields*, Physical Review E **70**, 066131 (2004).
- [10] G. Zhang, F. H. Stillinger, and S. Torquato, *The perfect glass paradigm: Disordered hyperuniform glasses down to absolute zero*, Scientific reports **6**, 36963 (2016).
- [11] S. Torquato, A. Scardicchio, and C. E. Zachary, *Point processes in arbitrary dimension from fermionic gases, random matrix theory, and number theory*, Journal of Statistical Mechanics: Theory and Experiment **2008**, P11019 (2008).
- [12] H. L. Montgomery, *The pair correlation of zeros of the zeta function*, **24**, 181 (1973).
- [13] M. L. Mehta, *Random matrices* (Elsevier, 2004).
- [14] R. Feynman and M. Cohen, *Energy spectrum of the excitations in liquid helium*, Physical Review **102**, 1189 (1956).
- [15] C. E. Zachary and S. Torquato, *Anomalous local coordination, density fluctuations, and void statistics in disordered hyperuniform many-particle ground states*, Physical Review E **83**, 051133 (2011).
- [16] D. Hexner and D. Levine, *Hyperuniformity of critical absorbing states*, Physical review letters **114**, 110602 (2015).
- [17] E. Tjhung and L. Berthier, *Hyperuniform density fluctuations and diverging dynamic correlations in periodically driven colloidal suspensions*, Physical review letters **114**, 148301 (2015).
- [18] J. Kim and S. Torquato, *Effect of imperfections on the hyperuniformity of many-body systems*, Physical Review B **97**, 054105 (2018).
- [19] J. Kim and S. Torquato, *Characterizing the hyperuniformity of ordered and disordered two-phase media*, Physical Review E **103**, 012123 (2021).

- [20] P. Debye and A. Bueche, *Scattering by an inhomogeneous solid*, Journal of Applied Physics **20**, 518 (1949).
- [21] P. Debye, H. R. Anderson, and H. Brumberger, *Scattering by an Inhomogeneous Solid. II. The Correlation Function and Its Application*, Journal of Applied Physics **28**, 679 (1957), <https://doi.org/10.1063/1.1722830>.
- [22] S. Torquato, *Diffusion spreadability as a probe of the microstructure of complex media across length scales*, Phys. Rev. E **104**, 054102 (2021).
- [23] H. Wang and S. Torquato, *Dynamic Measure of Hyperuniformity and Nonhyperuniformity in Heterogeneous Media via the Diffusion Spreadability*, Phys. Rev. Appl. **17**, 034022 (2022).
- [24] M. Skolnick and S. Torquato, *Simulated diffusion spreadability for characterizing the structure and transport properties of two-phase materials*, Acta Materialia **250**, 118857 (2023).
- [25] C. E. Maher, F. H. Stillinger, and S. Torquato, *Characterization of void space, large-scale structure, and transport properties of maximally random jammed packings of superballs*, Physical Review Materials **6**, 025603 (2022).
- [26] S. Prager, *Interphase transfer in stationary two-phase media*, Chemical Engineering Science **18**, 227 (1963).
- [27] S. Torquato and H. Haslach Jr, *Random heterogeneous materials: microstructure and macroscopic properties*, Appl. Mech. Rev. **55**, B62 (2002).
- [28] W. Man *et al.*, *Photonic band gap in isotropic hyperuniform disordered solids with low dielectric contrast*, Optics express **21**, 19972 (2013).
- [29] M. Florescu, S. Torquato, and P. J. Steinhardt, *Designer disordered materials with large, complete photonic band gaps*, Proceedings of the National Academy of Sciences **106**, 20658 (2009).
- [30] M. A. Klatt, P. J. Steinhardt, and S. Torquato, *Wave propagation and band tails of two-dimensional disordered systems in the thermodynamic limit*, Proceedings of the National Academy of Sciences **119**, e2213633119 (2022).
- [31] G. J. Aubry *et al.*, *Experimental tuning of transport regimes in hyperuniform disordered photonic materials*, Physical Review Letters **125**, 127402 (2020).
- [32] L. S. Froufe-Pérez, M. Engel, J. J. Sáenz, and F. Scheffold, *Band gap formation and Anderson localization in disordered photonic materials with structural correlations*, Proceedings of the National Academy of Sciences **114**, 9570 (2017).
- [33] O. Christogeorgos, H. Zhang, Q. Cheng, and Y. Hao, *Extraordinary directive emission and scanning from an array of radiation sources with hyperuniform disorder*, Physical Review Applied **15**, 014062 (2021).
- [34] R. D. Batten, F. H. Stillinger, and S. Torquato, *Novel low-temperature behavior in classical many-particle systems*, Physical review letters **103**, 050602 (2009).
- [35] R. D. Batten, F. H. Stillinger, and S. Torquato, *Interactions leading to disordered ground states and unusual low-temperature behavior*, Physical Review E **80**, 031105 (2009).
- [36] Q. Le Thien, D. McDermott, C. Reichhardt, and C. Reichhardt, *Enhanced pinning for vortices in hyperuniform pinning arrays and emergent hyperuniform vortex configurations with quenched disorder*, Physical Review B **96**, 094516 (2017).

- [37] S. Torquato, G. Zhang, and M. De Courcy-Ireland, *Hidden multiscale order in the primes*, Journal of Physics A: Mathematical and Theoretical **52**, 135002 (2019).
- [38] J. S. Brauchart, P. J. Grabner, and W. Kusner, *Hyperuniform point sets on the sphere: Deterministic aspects*, Constructive approximation **50**, 45 (2019).
- [39] J. S. Brauchart, P. J. Grabner, W. Kusner, and J. Ziefle, *Hyperuniform point sets on the sphere: probabilistic aspects*, Monatshefte für Mathematik **192**, 763 (2020).
- [40] S. Ghosh and J. L. Lebowitz, *Generalized stealthy hyperuniform processes: Maximal rigidity and the bounded holes conjecture*, Communications in Mathematical Physics **363**, 97 (2018).
- [41] D. Chen and S. Torquato, *Designing disordered hyperuniform two-phase materials with novel physical properties*, Acta Materialia **142**, 152 (2018).
- [42] D. Shechtman, I. Blech, D. Gratias, and J. W. Cahn, *Metallic phase with long-range orientational order and no translational symmetry*, Physical review letters **53**, 1951 (1984).
- [43] D. Levine and P. J. Steinhardt, *Quasicrystals: a new class of ordered structures*, Physical review letters **53**, 2477 (1984).
- [44] S. Ostlund and P. J. Steinhardt, *The Physics of Quasicrystals* (World Scientific Publishing Company, 1987).
- [45] S. Yu, C.-W. Qiu, Y. Chong, S. Torquato, and N. Park, *Engineered disorder in photonics*, Nature Reviews Materials **6**, 226 (2021).
- [46] Z. V. Vardeny, A. Nahata, and A. Agrawal, *Optics of photonic quasicrystals*, Nature photonics **7**, 177 (2013).
- [47] J. D. Joannopoulos, R. Meade, and J. N. Winn, *Photonic crystals*, Molding the flow of light (1995).
- [48] W. Man, M. Megens, P. J. Steinhardt, and P. M. Chaikin, *Experimental measurement of the photonic properties of icosahedral quasicrystals*, Nature **436**, 993 (2005).
- [49] M. C. Rechtsman, H.-C. Jeong, P. M. Chaikin, S. Torquato, and P. J. Steinhardt, *Optimized structures for photonic quasicrystals*, Physical review letters **101**, 073902 (2008).
- [50] W. Man *et al.*, *Photonic band gap in isotropic hyperuniform disordered solids with low dielectric contrast*, Optics express **21**, 19972 (2013).
- [51] M. Florescu, S. Torquato, and P. J. Steinhardt, *Complete band gaps in two-dimensional photonic quasicrystals*, Physical Review B **80**, 155112 (2009).
- [52] S. Aubry, C. Godrèche, and F. Vallet, *Incommensurate structure with no average lattice: an example of a one-dimensional quasicrystal*, Journal de Physique **48**, 327 (1987).
- [53] L. Kuipers and H. Niederreiter, *Uniform distribution of sequences* (Courier Corporation, 2012).
- [54] C. Lin, P. J. Steinhardt, and S. Torquato, *Hyperuniformity variation with quasicrystal local isomorphism class*, Journal of Physics: Condensed Matter **29**, 204003 (2017).
- [55] Penrose tiling online generator, 2023, Last update : 02/10/2023.
- [56] N. W. Ashcroft and N. D. Mermin, *Solid state physics* (Cengage Learning, 2022).
- [57] D. Levine and P. J. Steinhardt, *Quasicrystals. I. Definition and structure*, Physical Review B **34**, 596 (1986).

- [58] S. Torquato, *Hyperuniform states of matter*, Physics Reports **745**, 1 (2018).
- [59] S. Torquato and F. H. Stillinger, *New conjectural lower bounds on the optimal density of sphere packings*, Experimental Mathematics **15**, 307 (2006).
- [60] B. Lu and S. Torquato, *Local volume fraction fluctuations in heterogeneous media*, The Journal of chemical physics **93**, 3452 (1990).
- [61] S. Torquato, *Extraordinary Disordered Hyperuniform Multifunctional Composites*, arXiv preprint arXiv:2204.11345 (2022).
- [62] N. de Bruijn, *Algebraic theory of Penrose's non-periodic tilings of the plane. I, II: dedicated to G. Pólya*.
- [63] S. Torquato and G. Stell, *Microstructure of two-phase random media. V. The n-point matrix probability functions for impenetrable spheres*, The Journal of chemical physics **82**, 980 (1985).
- [64] S. Torquato, *Disordered hyperuniform heterogeneous materials*, Journal of Physics: Condensed Matter **28**, 414012 (2016).
- [65] S. Torquato and G. Stell, *Microstructure of two-phase random media. IV. Expected surface area of a dispersion of penetrable spheres and its characteristic function*, The Journal of chemical physics **80**, 878 (1984).